Under review for possible publication in

Knowledge-Aided and Adaptive Beam-Squint Aware MIMO-OFDM Radar Detectors for ISAC

Journal:	*IEEE Transactions on Communications*
Manuscript ID	TCOM-TLS-24-0379.R1
Manuscript Type:	Transactions Paper Submissions
Date Submitted by the Author:	17-Dec-2024
Complete List of Authors:	SARAÇ, UGUR; Orta Dogu Teknik Universitesi Elektrik ve Elektronik Muhendisligi Bolumu Guvensen, Gokhan M.; Orta Dogu Teknik Universitesi Elektrik ve Elektronik Muhendisligi Bolumu
Keyword:	Adaptive radar, Communication system performance, Interference suppression, MIMO systems, Radar clutter, Radar detection, Radar interference, Radar receivers, Radar signal processing, Signal processing

Knowledge-Aided and Adaptive Beam-Squint Aware MIMO-OFDM Radar Detectors for ISAC

Ugur B. Sarac, Gokhan M. Guvensen

Abstract—**Integrating radar and communication systems for economical use of hardware and spectrum resources is projected to be a crucial aspect of sixth-generation (6G) systems, leading to extensive research in the integrated sensing and communication (ISAC) area. In this article, we propose a radar detector structure for a multiple-input multiple-output (MIMO) ISAC system using orthogonal frequency-division multiplexing (OFDM) modulated waveforms. These waveforms are utilized to communicate with downlink (DL) users while receiving echoes from targets and clutter, in addition to separate OFDM-modulated uplink (UL) communication waveforms. The transmitter (Tx) and receiver (Rx) employ hybrid beamformers, with analog beamformers precisely designed to cover flat angular sectors. Tx and Rx beams are directed towards DL and UL users, respectively, with the possibility of overlapping or separate angular sectors. We introduce a Doppler-aware Code Bank (DACB) as the initial processing stage, thoroughly investigating the effects of Doppler mismatch. Following DACB, a sub-optimal sequential angle-range processing (SARP) method is proposed to maximize the output signal-to-interference-plus-noise ratio (SINR) while maintaining feasible processing. A two-variant detector scheme is proposed to address this processing's suboptimality. Four different detectors with varying complexities, including a fully adaptive detector, are introduced. The potential beam-squint (BS) effect due to increased bandwidth is also considered, and a subband approach is proposed to mitigate these effects. Simulation results for all four detectors, as well as a conventional 3-dimensional periodogram detector commonly used as a benchmark in the literature, are provided. The results demonstrate that the proposed detectors can significantly enhance SINR and the probability of detection, particularly when accounting for the coupling between the clutter Doppler and Tx OFDM symbols.**

Index Terms—**Radar and communication coexistence, MIMO-OFDM radar, detector structures, clutter channel model**

I. Introduction

There has been a significant interest in integrating radar and communication systems in the last few years, especially due to the increasing demand for sensing capability in communication-oriented systems. [1]–[5] are a few examples of valuable surveys about this research area. Among the numerous studies, there has yet to be a consensus on the name of the systems; integrated sensing and communication (ISAC), joint sensing and communication (JSAC) and *RadCom* are commonly used in the literature. We prefer to use ISAC to depict the integrated radar and communication system. On the other hand, there are both radar-centric studies, aiming to integrate communication capabilities into radar systems, and communication-centric studies, focusing on integrating sensing capabilities into communication systems. This study is one of the communication-centric ones, meaning that radar operation is done without negatively affecting the communication performance. Communication-centric ISAC can also occur in different ways. In a communication network, a transmitter (Tx) can simultaneously transmit and sense its environment using the signals coming from other transmitters. These systems are usually called perceptive networks and [6]–[8] are among the recent studies about this method of ISAC. On the other hand, a Tx can transmit and sense its environment at the same time utilizing its own transmitted signals, like classical radar systems. We focus on this type of communication-centric ISAC systems in this study, utilizing Orthogonal Frequency Division Multiplexing (OFDM) waveforms. OFDM is one of the most commonly used modulation schemes used in modern communication systems because it enables frequency-domain equalization which easily solves multipath channel problems, and its implementation is relatively easy. On the other hand, there are various studies which show that OFDM waveforms can also be used in sensing operation [4], [6]–[19].

In the literature for fifth-generation (5G) and sixth-generation (6G) systems, mm-wave multiple-input multiple-output (MIMO) communications are commonly focused due to the large communication band and high processing gain it provides. As expected, there are also several MIMO ISAC studies investigating sensing operation integrated into MIMO communication systems. In [20], a portion of the transmit (Tx) power is allocated for beam-scanning for radar detection. In [21], both transmit and receive (Rx) beamformers are optimized for sensing performance at a known target inside the cell-under-test (CUT). In [15], separate two antennas are utilized for radar signal transmission while a large antenna array continues MIMO communication and sensing. In [22], hybrid beamformers and compressive sensing are utilized for ISAC signal processing. In [23], radar detection is performed using the angle-sidelobes of the communication beams. These are only a few examples showing how different the MIMO ISAC approaches can be, mainly due to the large number of parameters, e.g. antenna and waveform structures, Tx and Rx beamformers, signal processing methods, etc. [24]–[31] are valuable works about MIMO ISAC using OFDM waveforms.

An aspect of the MIMO-OFDM ISAC systems is the effective bandwidth (W) of the system. In general, using as large W as possible is beneficial for both communication and sensing purposes; however, significantly increasing the W of the system can reduce the range resolution of the system so much that different antennas in the array can see different range responses coming from the same scatterer. In another

The authors are with Electrical and Electronics Engineering Dept., Middle East Technical University, Ankara, Turkey (e-mail: {usarac, guvensen}@metu.edu.tr)

perspective, a single scatterer can be seen at different angles in different subcarriers in a MIMO-OFDM detector. This beam-squint (BS) effect is investigated in [32] and has been shown to be effective for high carrier frequency over W ratios. In [9], this effect is mentioned and ignored as the W is selected to be relatively small. In [33], the beam-squint effect is intentionally used for searching purposes.

In this study, we focus on the radar detection performance of a MIMO-OFDM ISAC system under a realistic clutter model and the disruptive effects of beam-squint and uplink (UL) communication users. In our scenario, there are multiple scatterers in the sector of interest. The receiver gets the echoes of the transmitted signal from all of these scatterers but is interested in detecting only one of them. The scatterer that the receiver is trying to detect, mostly because it is a newcomer to the sector of interest, is called the intended target (IT). All other scatterers are also targets for the radar system but they are unwanted, this is why they are called unintended targets (UITs). UITs act like clutter, and they may be more powerful than the IT itself. The UITs also consist of multiple scattering centers, making sure that some part of them lies on fractional range and angle bins, making it harder to suppress them. The same interference model is used in [34] for a single-input, single-output (SISO) OFDM radar scenario, for reference. On the other hand, there are UL communication users and their signals are also disruptive to the radar operation. Besides, when the communication bandwidth becomes comparable to the center frequency, the beam-squint effect introduces a range-angle coupling, negatively affecting the MIMO radar performance. Last but not least, a Doppler mismatch in the filters or Doppler spread of UITs results in a symbol-dependent interference and undermines both angle and range processing if not handled correctly. The moving targets are usually related to the inter-carrier interference (ICI) problem in the literature. In [25], ICI is allowed and cleverly utilized to gain an advantage against range ambiguity problem. In [35], ICI problem is explained and mitigated by imposing a constraint on the linear dependency of modulation symbols. In [36], the same effect is mitigated by designing a special beamformer. ICI can be a problem when there are moving targets with high velocities, which is a well-known and investigated problem. However, Doppler mismatch in MIMO-OFDM ISAC systems poses another problem, signal-dependent interference, which undermines interference suppression even if the target velocities are small. In [37], this effect is mentioned and a modified element-wise division method is suggested to remove the negative effects of signal-dependent interference, losing the ability to apply further MIMO processing. Under all these disruptive effects, we propose a detector scheme that successfully suppresses the UITs and detects the IT.

The contributions of this study can be listed as:

- A mathematical model for the MIMO-OFDM channel under the disruptive effects of clutter, UL users, beam-squint effect and Doppler mismatch is constructed. The signal dependent disturbance on angle and range co-variances due to the Doppler mismatch is explained. A novel least-squares (LS) based approach is proposed to simultaneously apply classical Doppler processing and get rid of the signal dependency while preserving the dimensions required to apply further MIMO signal processing. The residual signal dependencies are also calculated and exploited for performance increase.
- A suboptimal knowledge-aided (KA) sequential angle-range processing (SARP) is proposed. Within SARP, theoretical signal-to-interference-plus-noise ratio (SINR) expressions and SINR maximizing filters are provided.
- A novel detector scheme is proposed to overcome the performance losses arising due to suboptimality. Its performance is evaluated in terms of SINR and probability of detection (P_d) metrics, including the comparison with benchmark detectors in the literature.
- Along with benchmark detectors, computationally softer detectors are proposed. Their mathematical backgrounds are provided. A novel, adaptive matched filter (AMF)-like [38] fully adaptive detector is also provided, which uses symbol-independent filters that do not require recalculation for multiple frames.

The rest of this paper is organized as follows. The system model including the MIMO channel and well-defined beamformers are explained in Section II. The proposed Doppler-Aware Code Bank (DACB), two-variant detector scheme, and SARP method are explained in detail in Section III. An explicit interpretation of the Doppler mismatch effect is also included in this section. In Section IV, the alternative filter implementations used in this study, arising in the two-variant detector scheme, are investigated. The simulation results and discussions are provided in Section V, followed by the concluding remarks in Section VI.

Notations: Regular letters, bold lowercase and bold uppercase letters denote scalars, vectors and matrices, respectively. $[.]^T, [.]^H, (.)^*, [.]^\#$, $\mathrm{Tr}\{.\}$, $\odot$, $\otimes$ and $\circledast$ denote transpose, Hermitian transpose, conjugate, pseudo-inverse, trace, element-wise multiplication, Kronecker product and Khatri-Rao (column-wise Kronecker) product operations, respectively. $\mathrm{diag}\{\mathbf{A}\}$ represents a vector including diagonal elements of $\mathbf{A}$ and $\mathrm{diag}\{\mathbf{a}\}$ represents a diagonal matrix $\mathbf{A}$ whose diagonal elements are $\mathbf{a}$. $[\mathbf{a}]_{(n)}$, $[\mathbf{A}]_{(n,m)}$ and $[\mathbf{A}]_{[n,m]}$ represents n^{th} element of vector $\mathbf{a}$, $(n,m)^{\text{th}}$ element of matrix $\mathbf{A}$ and $(n,m)^{\text{th}}$ block matrix inside matrix $\mathbf{A}$, respectively.

II. System Model

In this section, the mathematical model used in this article will be explained. In the first part, the MIMO channel is constructed and the necessary assumptions are made. In the second part, the analog beamformers are constructed and the different scenarios investigated in the article are explained.

A. MIMO Channel

The system in this study uses OFDM-modulated signals for both uplink (UL) and downlink (DL) communication purposes. For OFDM modulation, required cyclic prefix operations are assumed to be conducted successfully throughout the article. There are M OFDM symbols with duration T_s in a coherent processing interval (CPI), among which the reflected complex gain from any scatterer is highly correlated, enabling Doppler processing operations. On the other hand, the reflected complex gains from the scatterers are independent and identically distributed (iid) from CPI to CPI. The slow-time parameters of the scatterers (range, angle, velocity) are assumed to be the same through $\mathcal{T}$ CPIs, which are called frames, with duration T_f, in this article. In each OFDM symbol, there are $\bar{N}$ subcarriers, the distribution of which among communication users is not in the scope of this work. Among these $\bar{N}$ subcarriers, only N of them are used for radar purposes. For simplicity, these N subcarriers are assumed to be evenly distributed among all $\bar{N}$ subcarriers. Evenly spaced subcarriers enable OFDM processing to be done with DFT and IDFT operations, which are intuitive and easy to implement. Staggered distribution of subcarriers is not in the scope of this study. Since this article focuses on radar signal processing, the word 'subcarriers' will always mean the N subcarriers used for radar purposes, unless otherwise is clearly stated. The subcarrier spacing is Δf and the carrier frequency of n^{th} subcarrier is $f_n = f_1 + (n-1)\Delta f$, for $n = 1, 2, \cdots, N$. This means that total RF bandwidth is $W = N\Delta f$ and the center carrier frequency is $f_c = (f_1 + f_N)/2$. Corresponding to these subcarrier frequencies, the wavelength of n^{th} subcarrier is $\lambda_n = c/f_n$, where c is the speed of light in free space.

In our work, the UITs are considered to be large objects, possibly covering multiple range and angle resolution cells. For the sake of simplicity, the targets are approximated as collections of several point scattering centers. There are multiple UITs in the section of interest, each having a specific number of scatterers, which depends on the size of the corresponding UIT. A total of $\mathcal{K}$ scatterers exist in our scenario and in the rest of the paper, k is the index used for counting the scatterers. The k^{th} scatterer is assumed to be at range r_k, corresponding to a round-trip time of $\tau_k = 2r_k/c$, and has a radial velocity of v_k, corresponding to a normalized Doppler frequency of $\rho_k^{\mathcal{C}} = (2v_k/\lambda_c)T_s$[1], where $\lambda_c = c/f_c$ is the wavelength corresponding to the center carrier frequency.

We assume that there are N_t Tx antennas, N_r Rx antennas, D_t Tx RF chains and D_r Rx RF chains in the system. The Tx and Rx analog beamformers are denoted as $\mathbf{W}_t$ and $\mathbf{W}_r$, respectively. Using these variables, the frequency-domain MIMO channel matrix of the k^{th} scatterer for n^{th} subcarrier and m^{th} OFDM symbol can be written as:

$$\begin{aligned}\mathbf{H}_{knm} &= \alpha_{km} e^{j2\pi\rho_k^{\mathcal{C}} m}\mathbf{H}_{kn} \\ &= \alpha_{km} e^{j2\pi\rho_k^{\mathcal{C}} m}[\mathbf{W}_r^H \mathbf{a}_{kn}\mathbf{b}_{kn}^T \mathbf{W}_t^* e^{-j2\pi\tau_k\Delta f n}] \end{aligned} \quad (1)$$

where $\mathbf{a}_{kn}$ and $\mathbf{b}_{kn}$ are the receive and transmit steering vectors towards k^{th} scatterer at n^{th} subcarrier. $\mathbf{H}_{kn}$ is the $D_r \times D_t$ effective MIMO channel, including range and angle information of the scatterer after dimensions are reduced via analog beamforming, which is assumed to be stationary during M symbols; thus, it has no m index inside it. The random variable α_{km} is the reflected complex gain, depicting the complex amplitude and Doppler spread information of the scatterer, and $e^{j2\pi\rho_k^{\mathcal{C}} m}$ is for the mean Doppler shift of the scatterer. Note that α_{km} is a realization of a stationary slow-time random process with a given power spectral density (PSD) along the Doppler axis. Let's define

$$\boldsymbol{\alpha}_k \triangleq [\alpha_{k1}\, \alpha_{k2}\, \cdots\, \alpha_{kM}]^T, \mathbf{R}_k^{\boldsymbol{\alpha}} \triangleq \mathbb{E}\left\{\boldsymbol{\alpha}_k\boldsymbol{\alpha}_k^H\right\}, \quad (2)$$

where all of the diagonal elements of $\mathbf{R}_k^{\boldsymbol{\alpha}}$ are assumed to be equal to $\gamma_k^{\mathcal{C}} \triangleq \mathbb{E}\{|\alpha_{km}|^2\}$ because the average power of the returns from the scatterer is assumed to be the same for all M symbols. The off-diagonal elements of $\mathbf{R}_k^{\boldsymbol{\alpha}}$ determines the slow-time correlation properties of the k^{th} UIT[2].

The receive and transmit digital steering vectors towards a scatterer at angle θ from the boresight of ISAC antenna array at the n^{th} subcarrier are denoted as $\mathbf{a}_n(\theta)$ and $\mathbf{b}_n(\theta)$, which are $N_r \times 1$ and $N_t \times 1$ vectors, respectively. When the steering vectors are for k^{th} UIT or u^{th} user, we drop the angle and use simply $\mathbf{a}_{kn}$ or $\mathbf{b}_{un}$, for notational simplicity. The reader should understand that $\mathbf{a}_{kn}$ is the steering vector for k^{th} UIT, which is at angle θ_k. For example, if the antenna spacing is denoted as d, the receive steering vector can be written as:

$$\mathbf{a}_n(\theta) = [1 \quad e^{j\frac{2\pi}{\lambda_c}\frac{f_n}{f_c}d\sin\theta} \; \cdots \; e^{j\frac{2\pi}{\lambda_c}\frac{f_n}{f_c}D_r d\sin\theta}]^T \quad (3)$$

which depends on n due to the beam-squint effect. The (f_n/f_c) ratio determines how much the wave number shifts from its center value $(2\pi/\lambda_c)$, and its value is assumed to be unity in most scenarios. However, when W is comparable with f_c, it can be seen that $1-(W/2f_c) \leq (f_n/f_c) \leq 1+(W/2f_c)$. In other words, the beam-squint effect becomes more effective as the (f_c/W) ratio decreases.

Along with the clutter, a total of $\mathcal{U}$ single antenna communication users are in the section of interest. The u^{th} user sends the frequency domain communication symbol j_{unm} at n^{th} subcarrier in m^{th} symbol duration. Similar to the definition in (1), the effective channel vector for the u^{th} user at n^{th} subcarrier for m^{th} symbol is defined as:

$$\mathbf{g}_{unm} \triangleq \beta_{um} e^{j2\pi\rho_k^{\mathcal{S}} m}\mathbf{g}_{un} = \beta_{um} e^{j2\pi\rho_k^{\mathcal{S}} m}[\mathbf{W}_r^H \mathbf{a}_{un}] \quad (4)$$

where $\mathbf{g}_{un}$ is the $D_r \times 1$ effective SIMO channel including complex channel and angle information of the user after dimensions are reduced via analog beamforming. Note that this channel is also assumed to be stationary during M symbols, therefore it has no m index inside it. The random variable β_{um} is the received complex gain including the received power and Doppler spread information of the user channel and $e^{j2\pi\rho_k^{\mathcal{S}} m}$ is for the mean Doppler shift of the user[3]. Similar to (2),

$$\boldsymbol{\beta}_u \triangleq [\beta_{u1}\, \beta_{u2}\, \cdots\, \beta_{uM}]^T, \mathbf{R}_u^{\boldsymbol{\beta}} \triangleq \mathbb{E}\left\{\boldsymbol{\beta}_u\boldsymbol{\beta}_u^H\right\}, \quad (5)$$

[1] The Doppler shift is clearly dependent on the carrier frequency, and this results in different Doppler shifts occur in different subcarriers. However, when the center frequency f_c and bandwidth W of the system satisfies $f_c/W > M/2$, the maximum amount of Doppler shift across subcarriers becomes insignificant with respect to the Doppler resolution of the system. In this work, this inequality is assumed to be satisfied so that the normalized Doppler frequency is not dependent on subcarrier index.

[2] The random variable α_{km} is chosen to be a realization of a zero-mean complex Gaussian process, whose PSD function is Gaussian shaped with a variance of $(\sigma_k^{\mathcal{C}})^2$ and mean of zero. Such processes can be easily shown to have their autocorrelation matrix entries as $[\mathbf{R}_k^{\boldsymbol{\alpha}}]_{(i,j)} = \gamma_k^{\mathcal{C}} \exp(-2\pi^2(\sigma_k^{\mathcal{C}})^2(i-j)^2T_s^2)$.

[3] Since it is assumed that the synchronization is done for the SoI channel, the complex phase coming from propagation delay is not included in $\mathbf{g}_{unm}$. On the other hand, angular coherence time is assumed to be much larger than the CPI so that $\mathbf{g}_{un}$ and $\mathbf{H}_{kn}$ stay the same for M symbol durations.

where all of the the diagonal elements of $\mathbf{R}_u^{\beta}$ are assumed to be equal to $\gamma_u^{\mathcal{S}} \triangleq \mathbb{E}\{|\beta_{um}|^2\}$[4].

The $D_r \times 1$ received signal vector $\mathbf{y}_{nm}$ at the radar transceiver can be written as:

$$\mathbf{y}_{nm} = \underbrace{\mathbf{H}_{0nm}\mathbf{x}_{nm}}_{\mathbf{t}_{nm}} + \underbrace{\underbrace{\sum_{k=1}^{\mathcal{K}} \mathbf{H}_{knm}\mathbf{x}_{nm}}_{\mathbf{c}_{nm}} + \underbrace{\sum_{u=1}^{\mathcal{U}} \mathbf{g}_{unm} j_{unm}}_{\mathbf{s}_{nm}} + \mathbf{n}_{nm}}_{\boldsymbol{\psi}_{nm}} \tag{6}$$

where $\mathbf{x}_{nm}$ is the $D_t \times 1$ vector of Tx streams to DL users, and j_{unm} is the Rx symbol received from u^{th} UL user, at n^{th} subcarrier in m^{th} OFDM symbol. $\mathbf{t}_{nm}$, $\mathbf{c}_{nm}$, $\mathbf{s}_{nm}$ and $\mathbf{n}_{nm}$ are $D_r \times 1$ vectors who represent the received signal vector from intended target, total received signal vector from unintended targets (clutter), total received signal vectors from UL user signals, and noise, respectively. $\mathbf{H}_{0nm}$ is the effective MIMO channel for the intended target, whose expression is the same as the channels for UITs, given in (1). $\boldsymbol{\psi}_{nm}$ is the total additive interference on the intended target's response, namely the clutter, noise and the communication signal of interest (SoI). The noise vector $\mathbf{n}_{nm}$ is also defined after beamforming operation, namely it consists of D_r circularly symmetric zero-mean Gaussian random variables with covariance $\sigma_n^2 \mathbf{W}_r^H \mathbf{W}_r$. For notational simplicity, let's define:

$$\begin{aligned}
&\mathbf{X}_n \triangleq [\mathbf{x}_{n1}\, \mathbf{x}_{n2} \,\cdots\, \mathbf{x}_{nM}], && \mathbf{T}_n \triangleq [\mathbf{t}_{n1}\, \mathbf{t}_{n2} \,\cdots\, \mathbf{t}_{nM}],\\
&\mathbf{C}_n \triangleq [\mathbf{c}_{n1}\, \mathbf{c}_{n2} \,\cdots\, \mathbf{c}_{nM}], && \mathbf{S}_n \triangleq [\mathbf{s}_{n1}\, \mathbf{s}_{n2} \,\cdots\, \mathbf{s}_{nM}],\\
&\mathbf{N}_n \triangleq [\mathbf{n}_{n1}\, \mathbf{n}_{n2} \,\cdots\, \mathbf{n}_{nM}], && \boldsymbol{\Psi}_n \triangleq [\boldsymbol{\psi}_{n1}\, \boldsymbol{\psi}_{n2} \,\cdots\, \boldsymbol{\psi}_{nM}]\\
&\mathbf{Y}_n \triangleq [\mathbf{y}_{n1}\, \mathbf{y}_{n2} \,\cdots\, \mathbf{y}_{nM}], && \mathbf{J}_n \triangleq [\mathbf{j}_{1n}\, \mathbf{j}_{2n} \,\cdots\, \mathbf{j}_{\mathcal{U}n}]^T\\
&\mathbf{j}_{un} \triangleq [j_{un1}\, j_{un2} \,\cdots\, j_{unM}]^T
\end{aligned} \tag{7}$$

In this work, the slow-time processing gain is included in the transmit beamformer and not visible in the transmitted symbols. Therefore, $D_t \times M$ DL transmit symbol matrix $\mathbf{X}_n$ and $\mathcal{U} \times M$ UL transmit symbol matrix $\mathbf{J}_n$ are normalized accordingly. The average power per stream per subcarrier is selected to be unity, therefore $\text{Tr}\{\mathbb{E}\{\mathbf{X}_n\mathbf{X}_n^H\}\} = D_t$ and $\text{Tr}\{\mathbb{E}\{\mathbf{J}_n\mathbf{J}_n^H\}\} = \mathcal{U}$. To simplify the notation, we define four $M \times M$ diagonal matrices.

$$\mathbf{D}_k^{\mathcal{C}} \triangleq \text{diag}\{[1\; e^{j2\pi\rho_k^{\mathcal{C}}} \;\cdots\; e^{j2\pi(M-1)\rho_k^{\mathcal{C}}}]\}, \boldsymbol{\Lambda}_k^{\mathcal{C}} \triangleq \text{diag}\{\boldsymbol{\alpha}_k\} \tag{8}$$

are the matrices that represent the mean Doppler shift and the Doppler spread of the k^{th} scatterer. $\boldsymbol{\Lambda}_k^{\mathcal{C}}$ also includes the amplitude information of the k^{th} scatterer as $\boldsymbol{\alpha}_k$ is the reflected complex gain vector as described before. $\mathbf{D}_u^{\mathcal{S}}$ and $\boldsymbol{\Lambda}_u^{\mathcal{S}}$ have the same forms with $\mathbf{D}_k^{\mathcal{C}}$ and $\boldsymbol{\Lambda}_k^{\mathcal{C}}$ but they are for u^{th} communication user. Using (6), (7) and (8), $D_r \times M$ received symbol matrix $\mathbf{Y}_n$ is written and its elements can be defined as below:

$$\mathbf{Y}_n = \mathbf{T}_n + \underbrace{\underbrace{\sum_{k=1}^{\mathcal{K}} \mathbf{C}_{kn}}_{\mathbf{C}_n} + \underbrace{\sum_{u=1}^{\mathcal{U}} \mathbf{S}_{un}}_{\mathbf{S}_n} + \mathbf{N}_n}_{\boldsymbol{\Psi}_n}, \tag{9}$$

$$\begin{aligned}
&\mathbf{T}_n \triangleq \mathbf{H}_{0n}\mathbf{X}_n\mathbf{D}_0^{\mathcal{C}}\boldsymbol{\Lambda}_0^{\mathcal{C}}, \qquad \mathbf{C}_{kn} \triangleq \mathbf{H}_{kn}\mathbf{X}_n\mathbf{D}_k^{\mathcal{C}}\boldsymbol{\Lambda}_k^{\mathcal{C}},\\
&\mathbf{S}_{un} \triangleq \mathbf{g}_{un}\mathbf{j}_{un}^T\mathbf{D}_u^{\mathcal{S}}\boldsymbol{\Lambda}_u^{\mathcal{S}}.
\end{aligned} \tag{10}$$

It should be noted that (9) can be written because the MIMO channel matrix $\mathbf{H}_{kn}$ defined in (1) and SoI channel vector $\mathbf{g}_{un}$ are assumed to stay the same for the duration of M symbols. The formation of the received symbol matrix $\mathbf{Y}_n$ from its components is visually shown in Fig. 1.

B. Analog Beamformers

In this article, transmit and receive analog beamformers, $\mathbf{W}_t$ and $\mathbf{W}_r$, are adjusted separately. $\mathbf{W}_t(\mathbf{W}_r)$ is an $N_t \times D_t (N_r \times D_r)$ matrix, which is formed to cover the angular sector where DL(UL) users are located, and the UL and DL users may or may not be inside the same sector in a real-life application. Therefore, different scenarios in which the sectors fully overlap or do not overlap are investigated in the simulations section. Fig. 1 shows how the Tx and Rx sectors, DL and UL users, UITs, and the IT can be located in an example scenario of partially overlapping Tx-Rx sectors.

To reduce the power fluctuations inside the angular sectors, the columns of $\mathbf{W}_t(\mathbf{W}_r)$ are selected to be the eigenvectors of the intended angular sector corresponding to $D_t(D_r)$ largest eigenvalues. The transmit power constraint is adjusted so that $\text{Tr}\{\mathbf{W}_t\mathbf{W}_t^H\} = M$ is satisfied. This means that the system's slow-time processing gain is included through transmit beamforming, and the total transmit power is constrained. In the receiver part, however, to preserve the second-order stationarity of the noise after receive beamforming, $\mathbf{W}_r$ is scaled so that $\mathbf{W}_r^H\mathbf{W}_r = \mathbf{I}_{D_r}$ is satisfied.

III. Proposed Signal Processing Methods and Detector Structure

In this article, an IT is to be detected under the disruptive effects of UITs and UL users, by implementing knowledge-aided or adaptive detection strategies. Within the given system model, there are three domains in which detection will be conducted, namely range, angle and Doppler domains. To have a maximum-SINR filter for all domains, a $D_rNM \times D_rNM$ matrix must be known using the tracker or learned from the environment and its inverse must be taken in the filter implementation. In practical systems, this dimension is so large that neither effectively learning the matrix is possible before the channel decorrelates, nor is there enough processing power to implement this matrix inversion in real-time. Therefore, this article pursues a sub-optimal processing that separates range, angle and Doppler domains.

[4]The random variable β_{um} is chosen to be a realization of a zero-mean complex Gaussian process, whose PSD function is Gaussian shaped with a variance of $(\sigma_u^{\mathcal{S}})^2$ and mean of zero, whose autocorrelation matrix becomes $[\mathbf{R}_u^{\beta}]_{(i,j)} = \gamma_u^{\mathcal{S}} \exp(-2\pi^2(\sigma_u^{\mathcal{S}})^2(i-j)^2T_s^2)$.

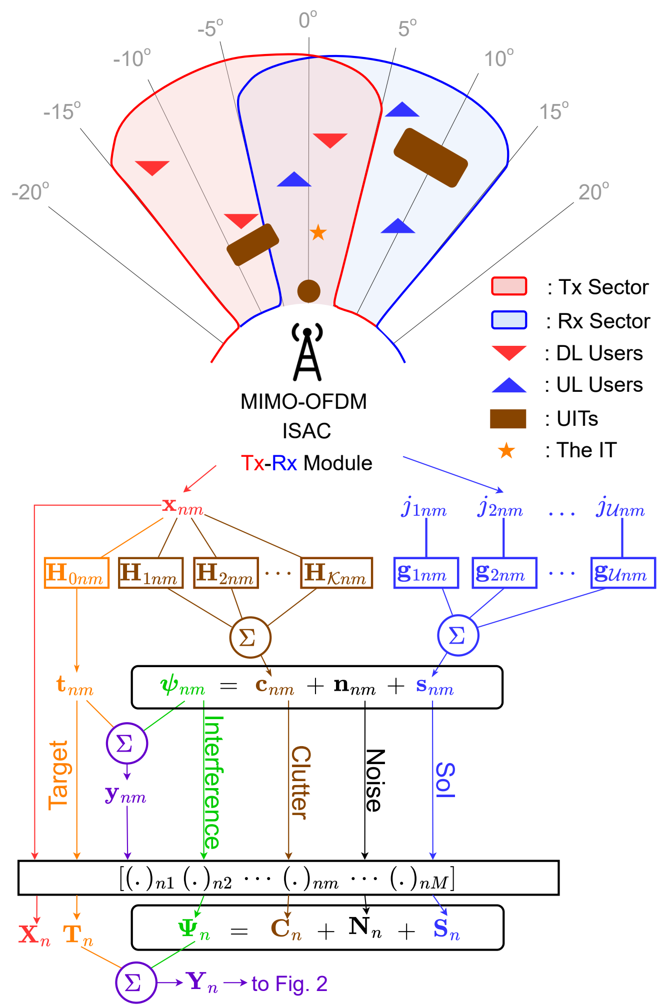

Fig. 1. Visualization of Tx-Rx sectors, DL and UL users, UITs and the IT in an example scenario of partially overlapping Tx-Rx sectors (top), and diagram of transmitted and received data matrices (bottom)

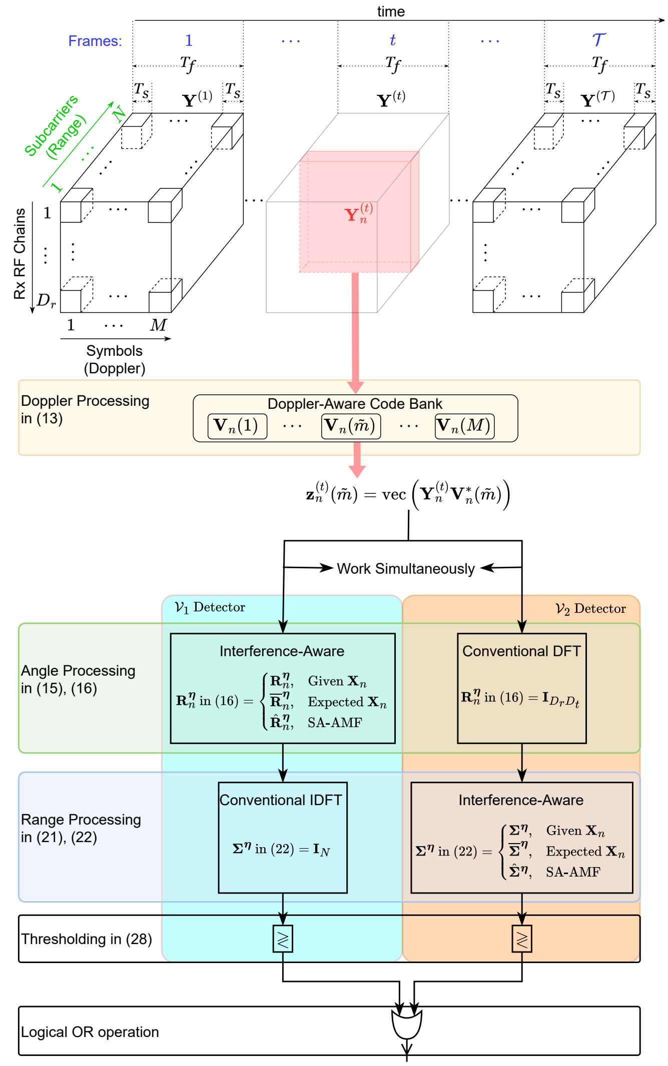

Fig. 2. Block diagram of proposed frame, symbol and subcarrier structures and signal processing, including the two-variant detector scheme

Due to possible beam-squint effects, MIMO processing should be done separately for each subcarrier, forcing angle processing to come before range processing. However, $D_r M \times D_r M$ matrix processing for each of the N subcarriers is still hard to work with. Besides, eliminating the Tx symbols at the first stage is crucial for OFDM radars, as the residual symbols would deteriorate the performance for the subsequent processing, as will be shown. For these reasons, a Doppler-Aware Code Bank (DACB) is proposed as the first stage of the processing, as in [9], [39]. With DACB, M symbols of transmitted data are combined separately for each Doppler CUT, and their dimension is reduced to $D_t < M$. It should be noted that for classical phased-array systems with $D_t = 1$, this processing would be equivalent to slow-time match filtering, namely coherent combination of M slow-time samples into one scalar for each of the D_r receive streams. In the MIMO case, the processing combines the slow-time samples into D_t dimensional vectors for each of the D_r receive streams, allowing transmit beamforming on the receiver side to utilize full MIMO gain of $D_r D_t$ [39], while easing the computations on the subsequent processing.

After applying DACB, we propose Sequential Angle-Range Processing (SARP) to combine data from $D_r D_t$ different streams and N different subcarriers into a single decision metric for the CUT. As described before, jointly and optimally combining $D_r D_t N$ amount of data is computationally burdensome, therefore MIMO processing is done separately for each subcarrier, and then the results for the subcarriers are combined. This sub-optimal method results in an SINR loss in some specific cases, therefore we propose a two-variant detector scheme to overcome this challenge. The details of this detector scheme are explained in Section III-B.

The output of the SARP stage is the decision metric for each CUT. This metric is then compared with the threshold and a decision is made on whether there is no detection (H_0 hypothesis) or detection (H_1 hypothesis). A block diagram showing the frame, symbol and subcarrier structures, the proposed signal processing methods starting from the observations $\mathbf{Y}_n$ up to the detector decisions, including the two-variant detector scheme, is given in Fig. 2.

In the following part of this section, the proposed processing method will be investigated in more detail. First, DACB will be explained and its interpretation will be provided. Next, why the proposed two-variant detector scheme is needed and how to apply it will be explained. Finally, the theoretical derivation of the SARP will be provided. Different detector structures shown in Fig. 2 will be explained in Section IV.

A. Doppler-Aware Code Bank (DACB)

When (9) and (10) are investigated, it is seen that to reach the channel $\mathbf{H}_{0n}$ of the IT for detection, the transmitted symbols and Doppler effects must be removed from the received signal. For SISO channels, where $\mathbf{H}_{0n}$ is a scalar for each subcarrier and OFDM symbol, the suppression of $\mathbf{X}_n$ can be done via Hadamard division, as in [16], [34]. However, in MIMO channels, as seen in (10), Hadamard division cannot give a good estimate of $\mathbf{H}_{0n}$. In this work, we estimate the channel using least-squares (LS) approach, as in [9], but we also conduct the Doppler processing at the same time.

For our preprocessing, and for the rest of the paper, we assume that the CUT is at $\tilde{n}^{\text{th}}$ range bin, $\tilde{m}^{\text{th}}$ Doppler bin and $\tilde{\theta}^{\text{th}}$ angle bin. In general, $\tilde{n}, \tilde{m}$ and $\tilde{\theta}$ can be fractional bins. Parentheses notation, e.g. $(\tilde{m})$, will be explicitly used when it is needed to clarify the dependence of a variable to any of the CUT parameters, like $\tilde{m}$ in this example. The $M \times D_t$ preprocessing matrix for $\tilde{m}^{\text{th}}$ Doppler bin is defined as:

$$\mathbf{V}_n(\tilde{m}) \triangleq \mathbf{D}_{\tilde{m}}^T(\mathbf{X}_n^{\#})^* = \mathbf{D}_{\tilde{m}}^T\mathbf{X}_n^T(\mathbf{X}_n^*\mathbf{X}_n^T)^{-1} \tag{11}$$

where $\mathbf{X}_n^{\#} = \mathbf{X}_n^H(\mathbf{X}_n\mathbf{X}_n^H)^{-1}$ is pseudo-inverse of $\mathbf{X}_n$ and

$$\mathbf{D}_{\tilde{m}} = \text{diag}\{1\, e^{j2\pi\tilde{m}/M}\, e^{j2\pi 2\tilde{m}/M} \cdots e^{j2\pi(M-1)\tilde{m}/M}\} \tag{12}$$

is the Doppler preprocessing matrix for $\tilde{m}^{\text{th}}$ Doppler bin.

After the preprocessing operation, the $D_r \times D_t$ MIMO channel estimate at n^{th} subcarrier for the CUT becomes:

$$\begin{aligned}
\widehat{\mathbf{H}}_n(\tilde{m}) &\triangleq \mathbf{Z}_n(\tilde{m}) \triangleq \mathbf{Y}_n\mathbf{D}_{\tilde{m}}^H\mathbf{X}_n^{\#} = \mathbf{Y}_n\mathbf{V}_n^* \\
&= \mathbf{T}_n\mathbf{V}_n^* + \mathbf{C}_n\mathbf{V}_n^* + \mathbf{S}_n\mathbf{V}_n^* + \mathbf{N}_n\mathbf{V}_n^* = \mathbf{T}_n\mathbf{V}_n^* + \mathbf{\Psi}_n\mathbf{V}_n^* \\
&= \mathbf{H}_{0n}\mathbf{X}_n\mathbf{D}_0^{\mathcal{C}}\mathbf{\Lambda}_0^{\mathcal{C}}\mathbf{D}_{\tilde{m}}\mathbf{X}_n^{\#} + \sum_{k=1}^{\mathcal{K}}\mathbf{H}_{kn}\mathbf{X}_n\mathbf{D}_k^{\mathcal{C}}\mathbf{\Lambda}_k^{\mathcal{C}}\mathbf{D}_{\tilde{m}}\mathbf{X}_n^{\#} \\
&+ \sum_{u=1}^{\mathcal{U}}\mathbf{g}_{un}\mathbf{j}_{un}^{\mathrm{T}}\mathbf{D}_u^{\mathcal{S}}\mathbf{\Lambda}_u^{\mathcal{S}}\mathbf{D}_{\tilde{m}}\mathbf{X}_n^{\#} + \mathbf{N}_n\mathbf{D}_{\tilde{m}}\mathbf{X}_n^{\#}
\end{aligned} \tag{13}$$

Here are some remarks about our preprocessing, DACB:

- The dimension of the processed data in each subcarrier is reduced from $D_r \times M$ to $D_r \times D_t$ with this preprocessing, meaning that M OFDM symbols are coherently combined but there are still D_t dimensions to achieve subsequent MIMO processing, explained in Section III-C.
- The Doppler processing and the elimination of Tx symbols are coupled. More specifically, $M \geq D_t$ must be satisfied to effectively find $\mathbf{X}_n^{\#}$ to eliminate the Tx symbols, but when M symbols are processed together, Doppler effects changes the slow-time codes of Tx symbols. This is a unique property of MIMO-OFDM ISAC systems.
- If the Doppler processing for the CUT matches the Doppler of the IT ($\mathbf{D}_{\tilde{m}} = (\mathbf{D}_0^{\mathcal{C}})^*$), and there is no Doppler spread of the target ($\mathbf{\Lambda}_0^{\mathcal{C}} = \mathbf{I}_M$), then $\mathbf{T}_n\mathbf{V}_n^* = \mathbf{H}_{0n}$, which means that the channel of the IT at the CUT to be used in hypothesis testing is extracted.
- However, it is almost always the case that there are other scatterers in the environment which have different Doppler shifts and Doppler spreads, meaning that there will be a Doppler mismatch between the preprocessing and some of the scatterers in the environment ($\mathbf{D}_{\tilde{m}} \neq (\mathbf{D}_k^{\mathcal{C}})^*$ and/or $\mathbf{\Lambda}_k^{\mathcal{C}} \neq \mathbf{I}_M$ for some ks). Therefore, the second term in (13) cannot be simplified to $\mathbf{H}_{kn}$.
- If $D_t = 1$, namely the system is not MIMO but a classical phased-array system, then $\mathbf{X}_n\mathbf{D}_k^{\mathcal{C}}\mathbf{\Lambda}_k^{\mathcal{C}}\mathbf{D}_{\tilde{m}}\mathbf{X}_n^{\#}$ would be a scalar and the Doppler mismatch effect would not change the matrix structure of the clutter channel $\mathbf{H}_{kn}$ (UIT channels). However in MIMO systems, $\mathbf{H}_{kn}$ is multiplied from right with a matrix dependent on $\mathbf{X}_n$. This means that both angle and range information of the clutter are disturbed due to the Doppler mismatch in the preprocessing stage.
- As will be shown in (27), Doppler mismatch results in a Hadamard product-based disturbance in the range response of the scatterers. If this effect is taken into consideration, it acts as a diversity in Doppler domain and results in an increased output SINR (due to clutter suppression in Doppler domain). If this effect is overseen, it makes the clutter spread over the whole range spectrum, disables the range processing to suppress the clutter and results in a reduced output SINR.
- Doppler mismatch also affects the angular response of the scatterers, which can be seen when (19) is investigated, but the details are not written in this paper for the sake of neatness. The angular responses of the scatterers are linearly transformed due to the Doppler mismatch, which is also dependent on $\mathbf{X}_n$. Similar to the range processing part, detectors that take this effect into consideration achieve greater clutter suppression with MIMO filters.

B. Two-variant detector scheme

As explained before, DACB is followed by sequential MIMO and range processing. In practice, using max-SINR filters for both MIMO and range processings separately rather than using a joint max-SINR filter can cause a performance degradation. This is because the first filter in the sequence of filters, which is MIMO filter in our case, tries to suppress the clutter without considering that there will be another filter which can also suppress the clutter. If the IT is angularly close to the clutter, it would also be suppressed to a level under the noise level, and range processing cannot do anything to increase the SINR. In other words, first stage can lose the useful information that second stage can exploit in order to maximize its own output SINR. Using jointly-optimal range-angle filter can solve this problem easily, but this is not realizable in real-time as explained before. Therefore, we propose another suboptimal detector scheme in order to get rid of this specific problematic case.

We propose a detection scheme in which two different detectors are utilized simultaneously and their detection results are combined (with or operation). The first set of detectors, identified with $\mathcal{V}_1$, use an interference-aware processing in MIMO domain and conventional IDFT processing in range domain. The other set of detectors, identified with $\mathcal{V}_2$, use conventional DFT processing in MIMO domain and an interference-aware processing in range domain. This way, in both angle and range domains, the max-SINR filters can use all useful information about the interference, not affecting each other. The working principle of this detector scheme is shown in Fig. 2. Details of the interference-aware processing are given in Section III-C.

1) $\mathcal{V}_1$ detectors: The first set of detectors, which we call as $\mathcal{V}_1$ detectors, uses conventional IDFT for range processing. In other words, they select the range covariance matrix as identity matrix when calculating the range processing filter $\mathbf{u}$ in (22), in Section III-C. For MIMO processing part, three different filter implementations are investigated in this paper, as shown in Fig. 2. It should be noted that if the beam-squint effect is neglected, the order of MIMO and range processings of $\mathcal{V}_1$ detectors can be changed. In other words, without the beam-squint effects, conventional IDFT in range domain can be applied directly to $\{\mathbf{Z}_n\}$ and MIMO processing can be applied to each subcarrier afterward, without any change in the resultant detection metrics.

2) $\mathcal{V}_2$ detectors: The second set of detectors in our two-variant detector scheme, $\mathcal{V}_2$ detectors, use conventional DFT for MIMO processing. Namely, they select the angle covariance matrix as identity matrix in (16), in Section III-C. For range processing part, three different filter implementations are investigated in this paper, as shown in Fig. 2.

It should be noted that the two-variant detector scheme does not suggest only one of these detectors is selected and utilized. Instead, both detectors are working simultaneously and their decisions are combined. In general, $\mathcal{V}_1$ detectors are better at suppressing clutter in angle domain, and $\mathcal{V}_2$ detectors are better at suppressing clutter in range domain. When utilized together, they compensate for each other's weaknesses and suppress clutter effectively in both domains.

C. *Interference-Aware Sequential Angle-Range Processing*

As the next step of processing, we apply spatial processing for each subcarrier to resolve any beam-squint effect before combining the symbols in range domain. As seen in Fig. 2, we propose three different filters for spatial processing for $\mathcal{V}_1$ detectors and three different filters for range processing for $\mathcal{V}_2$ detectors. These filters are common in the sense that they are all interference-aware, meaning that they use the prior covariance information of the UITs, possibly coming from the tracker or obtained from the training data adaptively, with the aim of increasing output SINR. What differentiates the proposed filters from each other is the covariance matrices they use. The conventional DFT and IDFT filters do not depend on any information about UITs; however, they can be written as a special case of our proposed filters when the covariances are selected to be identity matrices. Therefore, the filter structures explained in this section will be the basis for all detectors that are investigated in this study, only difference between them being the selection of covariance matrices.

The spatial filter at each subcarrier is derived as follows. At each subcarrier, the MIMO channel is a $D_r \times D_t$ matrix and to jointly use all elements of this matrix, vectorization is used. Define the vectorized forms of the matrices in (13) as:

$$\begin{aligned} \boldsymbol{\phi}_n &\triangleq \mathrm{vec}\{\mathbf{T}_n \mathbf{V}_n^*\} \triangleq \overline{\mathbf{V}}_n^H \,\mathrm{vec}\{\mathbf{T}_n\}, \\ \boldsymbol{\eta}_n &\triangleq \mathrm{vec}\{\boldsymbol{\Psi}_n \mathbf{V}_n^*\} \triangleq \overline{\mathbf{V}}_n^H \,\mathrm{vec}\{\boldsymbol{\Psi}_n\}, \\ \mathbf{z}_n &\triangleq \mathrm{vec}\{\mathbf{Z}_n\} = \boldsymbol{\phi}_n + \boldsymbol{\eta}_n \end{aligned} \tag{14}$$

where $\overline{\mathbf{V}}_n = \mathbf{V}_n \otimes \mathbf{I}_{D_r}$ is $MD_r \times D_t D_r$ effective preprocessing matrix which is defined for notational simplicity in the rest of the paper. Let's define the result of the processing at the n^{th} subcarrier as:

$$r_n = [\mathbf{r}]_{(n)}(\tilde{m}, \tilde{\theta}) = \boldsymbol{\omega}_n^H(\tilde{m}, \tilde{\theta})\,\mathrm{vec}\{\mathbf{Z}_n\} \triangleq \boldsymbol{\omega}_n^H \mathbf{z}_n(\tilde{m}) \tag{15}$$

where $\boldsymbol{\omega}_n$ is the spatial filter applied to n^{th} subcarrier after the DACB and $\mathbf{r}$ is the $N \times 1$ result of the processing whose n^{th} element is r_n. $\boldsymbol{\omega}_n$ can be formulated as:

$$\boldsymbol{\omega}_n = \frac{(\mathbf{R}_n^{\boldsymbol{\eta}})^{-1}(\tilde{m})\mathbf{p}_n(\tilde{\theta})}{\mathbf{p}_n^H(\tilde{\theta})(\mathbf{R}_n^{\boldsymbol{\eta}})^{-1}(\tilde{m})\mathbf{p}_n(\tilde{\theta})} \tag{16}$$

where $\mathbf{p}_n(\tilde{\theta})$ is the $D_t D_r \times 1$ spatial steering vector towards $\tilde{\theta}$ and $\mathbf{R}_n^{\boldsymbol{\eta}}(\tilde{m})$ is the $D_t D_r \times D_t D_r$ spatial covariance matrix of the preprocessed received frame under H_0. It should be noted that $\boldsymbol{\omega}_n$ is the minimum variance distortionless response (MVDR) filter [40], meaning that it minimizes the total average power at the output while making the output unity when $\mathbf{z}_n$ happens to be equal to $\mathbf{p}_n$. Assuming that the IT is at angle $\tilde{\theta}$, the spatial steering vector towards the IT is:

$$\begin{aligned} \mathbf{p}_n(\tilde{\theta}) &= \mathrm{vec}\{\mathbf{W}_r^H \mathbf{a}_n(\tilde{\theta})(\mathbf{b}_n(\tilde{\theta}))^T \mathbf{W}_t^*\} \\ &= (\mathbf{W}_t^H \mathbf{b}_n(\tilde{\theta})) \otimes (\mathbf{W}_r^H \mathbf{a}_n(\tilde{\theta})), \end{aligned} \tag{17}$$

which is the spatial response coming from a hypothetical point target at angle $\tilde{\theta}$ in vectorized form. The spatial covariance matrix of $\mathbf{z}_n$ under H_0, namely when there is no IT contamination, can be defined as:

$$\begin{aligned} &\mathbf{R}_n^{\boldsymbol{\eta}}(\tilde{m}) \triangleq \mathbb{E}\{\mathbf{z}_n(\tilde{m})\mathbf{z}_n^H(\tilde{m})|H_0\} \triangleq \mathbb{E}\{\boldsymbol{\eta}_n(\tilde{m})\boldsymbol{\eta}_n^H(\tilde{m})\} \\ &= \overline{\mathbf{V}}_n^H \mathbb{E}\left\{\mathrm{vec}\{\boldsymbol{\Psi}_n\}\,\mathrm{vec}\{\boldsymbol{\Psi}_n\}^H\right\}\overline{\mathbf{V}}_n \triangleq \overline{\mathbf{V}}_n^H \mathbf{R}_n^{\psi} \overline{\mathbf{V}}_n \end{aligned} \tag{18}$$

where $\mathbf{R}_n^{\psi}$ is the $MD_r \times MD_r$ spatial covariance matrix of the interference before the DACB. It should be noted that both $\mathbf{R}_n^{\psi}$ and $\mathbf{R}_n^{\boldsymbol{\eta}}$ are dependent on $\mathbf{X}_n$. Therefore, $\boldsymbol{\omega}_n$ must be calculated for each Tx symbol sequence $\mathbf{X}_n$, which can be computationally burdensome. To ease the calculations, $\boldsymbol{\omega}_n$ can be computed with the expectation of the $\mathbf{R}_n^{\boldsymbol{\eta}}$ over $\mathbf{X}_n$, with a performance loss. When the transmitted symbols $\mathbf{X}_n$ are given, $\mathbf{R}_n^{\psi}$ can be written as in (19). The derivation of (19) and the expectation of $\mathbf{R}_n^{\boldsymbol{\eta}}$ over $\mathbf{X}_n$ are provided in the extended version of this paper [41]. When (18) and (19) are investigated, it can be seen that the range information of the scatterers, which is the scalar phase component in the channel $\mathbf{H}_{kn}$ defined in (1), is canceled out in $\mathbf{R}_n^{\boldsymbol{\eta}}$. This means that the proposed MIMO processing has no information about the range profile of the interference.

As the last step of processing, we apply an $N \times 1$ temporal filter $\mathbf{u}$ on $\mathbf{r}$ to get our decision metric ξ as:

$$\xi(\tilde{n}, \tilde{m}, \tilde{\theta}) = \left|\mathbf{u}^H \mathbf{r}\right|^2. \tag{21}$$

$$\mathbf{R}_n^{\boldsymbol{\psi}} = \sum_{k=1}^{\mathcal{K}} (\mathbf{I}_M \otimes \mathbf{H}_{kn})(\mathbf{I}_M \circledast (\mathbf{X}_n \mathbf{D}_k^{\mathcal{C}}))\mathbf{R}_k^{\boldsymbol{\alpha}}(\mathbf{I}_M \circledast (\mathbf{X}_n \mathbf{D}_k^{\mathcal{C}}))^H (\mathbf{I}_M \otimes \mathbf{H}_{kn})^H + \sum_{u=1}^{\mathcal{U}} \frac{\gamma_u^{\mathcal{S}}}{M}(\mathbf{I}_M \otimes \mathbf{g}_{un}\mathbf{g}_{un}^H) + \sigma_n^2 \mathbf{I}_{MD_r} \tag{19}$$

$$\mathbf{R}_{n_1 n_2}^{\boldsymbol{\psi}} = \begin{cases} \mathbf{R}_{n_1}^{\boldsymbol{\psi}}, & \text{if } n_1 = n_2 \\ \sum\limits_{k=1}^{\mathcal{K}} (\mathbf{I}_M \otimes \mathbf{H}_{kn_1})(\mathbf{I}_M \circledast (\mathbf{X}_{n_1} \mathbf{D}_k^{\mathcal{C}}))\mathbf{R}_k^{\boldsymbol{\alpha}}(\mathbf{I}_M \circledast (\mathbf{X}_{n_2} \mathbf{D}_k^{\mathcal{C}}))^H (\mathbf{I}_M \otimes \mathbf{H}_{kn_2})^H, & \text{if } n_1 \neq n_2 \end{cases} \tag{20}$$

The temporal filter $\mathbf{u}$ can be written as:

$$\mathbf{u}(\tilde{n}, \tilde{m}, \tilde{\theta}) = \frac{\boldsymbol{\Sigma}^{\boldsymbol{\eta}^{-1}}(\tilde{m}, \tilde{\theta})\mathbf{q}(\tilde{n})}{\sqrt{\mathbf{q}^H(\tilde{n})\boldsymbol{\Sigma}^{\boldsymbol{\eta}^{-1}}(\tilde{m}, \tilde{\theta})\mathbf{q}(\tilde{n})}} \tag{22}$$

where $\mathbf{q}(\tilde{n})$ is the $N \times 1$ range steering vector towards $\tilde{n}$ and $\boldsymbol{\Sigma}^{\boldsymbol{\eta}}(\tilde{m}, \tilde{\theta})$ is defined as the $N \times N$ range covariance matrix of the preprocessed and spatial filtered received frame, again without the IT contamination. It should be noted that the normalization in $\mathbf{u}$ makes sure that $\mathbb{E}\{\xi | H_0\} = 1$ if $\boldsymbol{\Sigma}^{\boldsymbol{\eta}} = \mathbb{E}\{\mathbf{r}\mathbf{r}^H | H_0\}$ is indeed satisfied. Assuming that the IT is at a range corresponding to $\tilde{n}^{\text{th}}$ subcarrier (range bin), n^{th} element of the temporal steering vector towards the IT is:

$$[\mathbf{q}(\tilde{n})]_n = e^{-j(2\pi/N)\tilde{n}n}\boldsymbol{\omega}_n^H \mathbf{p}_n = e^{-j(2\pi/N)\tilde{n}n}, \tag{23}$$

which is the temporal response coming from a hypothetical point target at $\tilde{n}^{\text{th}}$ range cell. The range covariance matrix of $\mathbf{r}$ under H_0 can be defined as:

$$\boldsymbol{\Sigma}^{\boldsymbol{\eta}}(\tilde{m}, \tilde{\theta}) \triangleq \mathbb{E}\{\mathbf{r}(\tilde{m}, \tilde{\theta})\mathbf{r}^H(\tilde{m}, \tilde{\theta}) | H_0\} \tag{24}$$

When the transmitted symbols for all subcarriers, namely $\mathbf{X}_1, \mathbf{X}_2, \cdots, \mathbf{X}_N$, are given, $(n_1, n_2)^{\text{th}}$ element of $\boldsymbol{\Sigma}^{\boldsymbol{\eta}}$ can be written as:

$$\begin{aligned} [\boldsymbol{\Sigma}^{\boldsymbol{\eta}}]_{(n_1, n_2)} &= \mathbb{E}\left\{\boldsymbol{\omega}_{n_1}^H \mathbf{z}_{n_1} \mathbf{z}_{n_2}^H \boldsymbol{\omega}_{n_2} | H_0, \mathbf{X}_{n_1}, \mathbf{X}_{n_2}\right\} \\ &= \boldsymbol{\omega}_{n_1}^H \mathbb{E}\left\{\boldsymbol{\eta}_{n_1}\boldsymbol{\eta}_{n_2}^H | \mathbf{X}_{n_1}, \mathbf{X}_{n_2}\right\}\boldsymbol{\omega}_{n_2} \triangleq \boldsymbol{\omega}_{n_1}^H \mathbf{R}_{n_1 n_2}^{\boldsymbol{\eta}} \boldsymbol{\omega}_{n_2} \end{aligned} \tag{25}$$

where $\mathbf{R}_{n_1 n_2}^{\boldsymbol{\eta}}$ is the $D_t D_r \times D_t D_r$ spatial cross-correlation matrix of the preprocessed interference terms between ${n_1}^{\text{st}}$ and ${n_2}^{\text{nd}}$ subcarriers, which can also be written as:

$$\begin{aligned} \mathbf{R}_{n_1 n_2}^{\boldsymbol{\eta}} &= \overline{\mathbf{V}}_{n_1}^H \mathbb{E}\left\{\text{vec}\{\boldsymbol{\Psi}_{n_1}\}\,\text{vec}\{\boldsymbol{\Psi}_{n_2}\}^H\right\}\overline{\mathbf{V}}_{n_2} \\ &= \overline{\mathbf{V}}_{n_1}^H \mathbf{R}_{n_1 n_2}^{\boldsymbol{\psi}} \overline{\mathbf{V}}_{n_2} \end{aligned} \tag{26}$$

where $\mathbf{R}_{n_1 n_2}^{\boldsymbol{\psi}}$ is the $D_t D_r \times D_t D_r$ spatial cross-correlation matrix of the raw interference terms between ${n_1}^{\text{st}}$ and ${n_2}^{\text{nd}}$ subcarriers, whose closed form expression is given in (20). The derivation of (20) and the expectation of $\mathbf{R}_{n_1 n_2}^{\boldsymbol{\eta}}$ over $\mathbf{X}_{n_1}$ and $\mathbf{X}_{n_2}$ are given in the extended version of this paper [41]. It should be noted that both $\mathbf{R}_{n_1 n_2}^{\boldsymbol{\psi}}$ and $\mathbf{R}_{n_1 n_2}^{\boldsymbol{\eta}}$ are also dependent on $\mathbf{X}_n$. Therefore, $\mathbf{u}$ must be calculated for each Tx symbol sequence $\mathbf{X}_n$ to get the range filter with maximum output SINR. To ease the calculations, $\mathbf{u}$ can be computed with the expectation of the $\boldsymbol{\Sigma}^{\boldsymbol{\eta}}$ over $\mathbf{X}_n$, with a performance loss.

When (1), (26) and (20) are investigated, it can be seen that the range information of the scatterers are carried in the off-diagonal elements of the $\boldsymbol{\Sigma}^{\boldsymbol{\eta}}$ matrix. More explicitly, the contribution from the k^{th} scatterer to the $(n_1, n_2)^{\text{th}}$ element of $\boldsymbol{\Sigma}^{\boldsymbol{\eta}}$ is $e^{-j2\pi\tau_k \Delta f (n_1 - n_2)}$ times another scalar which does not depend on the range of the corresponding scatterer. If we define $\mathbf{q}_k^{\mathcal{C}}$ to be the range response of the k^{th} scatterer where $\left[\mathbf{q}_k^{\mathcal{C}}\right]_n \triangleq e^{-j2\pi\tau_k \Delta f n}$ for $n = 0, 1, \cdots, N-1$, then

$$\boldsymbol{\Sigma}^{\boldsymbol{\eta}} = \sum_{k=1}^{\mathcal{K}} \mathbf{q}_k^{\mathcal{C}}(\mathbf{q}_k^{\mathcal{C}})^H \odot \mathbf{A}_k(\tilde{m}, \tilde{\theta}, \mathbf{X}_n) \tag{27}$$

where $\mathbf{A}_k$, which depends on $\tilde{m}, \tilde{\theta}, \mathbf{X}_n$ for all subcarriers, as well as the angle and Doppler properties of k^{th} scatterer but not the range of it, can be found easily but not written here for the sake of neatness. It should be noted that if there were only a single scatterer with no Doppler spread and the Doppler processing perfectly matched the Doppler of the scatterer, $\mathbf{A}_k$ would become an all-ones matrix and $\boldsymbol{\Sigma}^{\boldsymbol{\eta}}$ would become a rank-1 matrix which includes the range information of the scatterer. However, in a more realistic scenario, even a slight Doppler spread or a Doppler mismatch between the DACB and any of the scatterers results in an increase in the rank of $\mathbf{A}_k$ and $\boldsymbol{\Sigma}^{\boldsymbol{\eta}}$. In other words, the Doppler mismatch causes the range response of the scatterers, which would be impulsive otherwise, to spread over the whole range spectrum. In addition to this, this spread depends on the transmitted symbols $\mathbf{X}_n$. As a consequence, if $\boldsymbol{\Sigma}^{\boldsymbol{\eta}}$ matrix information is not used at the receiver side, the range information of the scatterers cannot be learned and the output SINR is reduced when there is Doppler mismatch. On the other hand, if the $\boldsymbol{\Sigma}^{\boldsymbol{\eta}}$ matrix is exploited at the receiver side, which requires tracker information and a relatively high computation power, the effects of the Doppler mismatch can be resolved and due to the increased rank of $\boldsymbol{\Sigma}^{\boldsymbol{\eta}}$, output SINR can be increased even more with respect to the case with no Doppler mismatch.

After the decision metric ξ is determined, it is compared to the pre-determined CFAR threshold γ_{th} to make the decision:

$$\xi(\tilde{n}, \tilde{m}, \tilde{\theta}) \underset{H_0}{\overset{H_1}{\gtrless}} \gamma_{th}, \tag{28}$$

where γ_{th} can be adaptively found using previous uncontaminated frames of data. A similar threshold map calculation is explained in detail in [34] for SISO OFDM ISAC systems. In this study, Tx symbols cannot be completely eliminated as explained before, therefore instantaneous thresholds depend on Tx symbols. However, the system can calculate average thresholds over Tx symbols and use them in the long term as the clutter is assumed to be stationary for multiple frames.

As a metric to compare the processing methods fairly, the output SINR and the range covariance matrix of the IT after

MIMO processing are defined as:

$$\mathbf{\Sigma}^{\phi}(\tilde{m},\tilde{\theta}) \triangleq \mathbb{E}\{\mathbf{r}\mathbf{r}^H|H_1\} - \mathbb{E}\{\mathbf{r}\mathbf{r}^H|H_0\}, \tag{29}$$

$$\mathrm{SINR} = \frac{\mathbf{u}^H\mathbf{\Sigma}^{\phi}\mathbf{u}}{\mathbf{u}^H\mathbf{\Sigma}^{\boldsymbol{\eta}}\mathbf{u}}. \tag{30}$$

It should be noted that in this section, the filters in (16) and (22) are written for the benchmark interference-aware detector. In the later sections, filter calculations will remain the same but the covariances used in them will change depending on the filter type. In the next section, different implementations of filters used in this study will be investigated.

IV. Alternative Filter Implementations In The Proposed Detector Structure

In this section, alternative filter implementations used in this article will be investigated. In the first subsection, seven different filters investigated in this study will be explained. In the next subsection, the interpretation of these filters with respect to the beam-squint effect will be provided.

A. *Alternative Filter Implementations*

There are seven different filter implementations investigated in this article. The first three filters correspond to three different $\mathcal{V}_1$ detectors. As can be seen in Fig. 2, only the angular covariance matrix in the MIMO filters is different in these three detectors. The next three filters correspond to three different $\mathcal{V}_2$ detectors. As it can be seen in Fig. 2, only the range covariance matrix in the temporal filters is different in these three detectors. The final filter corresponds to the benchmark 3-D periodogram detector, which uses conventional DFT and IDFT for MIMO and range processing, respectively. This detector is not shown in Fig. 2, but it can be seen as a special case of either $\mathcal{V}_1$ or $\mathcal{V}_2$ detector, when the corresponding covariance matrix is selected as identity matrix.

1) KA-SARP Given $\mathbf{X}_n$, $\mathcal{V}_1$ detector: This detector utilizes the proposed MIMO filter structure in (16) using the true knowledge of interference angular covariance matrix $\mathbf{R}_n^{\boldsymbol{\eta}}$, which can be supplied to the detector as target maps from trackers. The MIMO filter $\boldsymbol{\omega}_n$ is constructed for each subcarrier and each Tx symbol $\mathbf{X}_n$, which requires $D_rD_t \times D_rD_t$ matrix inversions N times per frame. In each subcarrier, the angular filter depends on the transmitted symbols. Therefore, this detector is denoted as "Given $\mathbf{X}_n$". This detector is the only one in this paper that uses different MIMO filters for each subcarrier due to changing Tx symbols $\mathbf{X}_n$. This unique property results in an improved angular interference suppression with a high computational cost. This detector must be used only if the angular information of UITs is available and there is not a constraint on the computational power.

2) KA-SARP with Expected $\mathbf{X}_n$, $\mathcal{V}_1$ detector: As mentioned previously, the true covariances $\mathbf{R}, \mathbf{\Sigma}$ and thus the max-SINR filters $\boldsymbol{\omega}, \mathbf{u}$ depend on the symbol sequence $\mathbf{X}_n$ at each subcarrier. In order to ease the calculation of the filters, expected filters over symbols $\mathbf{X}_n$ at each subcarrier can be found. The calculations of the expectations are given in the extended version of this paper [41]. The expectations of $\mathbf{R}_n^{\boldsymbol{\eta}}$ and $\mathbf{\Sigma}^{\boldsymbol{\eta}}$ over $\mathbf{X}_n$ are denoted as $\overline{\mathbf{R}}_n^{\boldsymbol{\eta}}$ and $\overline{\mathbf{\Sigma}}^{\boldsymbol{\eta}}$, respectively. Since the expectations are taken over $\mathbf{X}_n$ symbols, this detector is denoted as "Expected $\mathbf{X}_n$".

Expected $\mathbf{X}_n$, $\mathcal{V}_1$ detector forms the max-SINR MIMO filter $\boldsymbol{\omega}_n$ in (16) by using $\overline{\mathbf{R}}_n^{\boldsymbol{\eta}}$ instead of $\mathbf{R}_n^{\boldsymbol{\eta}}$. The angular correlation time is assumed to be much larger than the OFDM frame duration. Therefore, the filters in Expected $\mathbf{X}_n$, $\mathcal{V}_1$ detector can be calculated only once in several frames. This detector can be used when the angular information of UITs is available but there is only a limited computational power.

3) Fully Adaptive AMF-like SARP with SA, $\mathcal{V}_1$ detector: The previously explained detectors are knowledge-aided, meaning that their performances significantly depend on the true knowledge of the interference covariance matrices. As an alternative processing method, we propose a fully adaptive filter learning the interference covariance using only $\mathcal{T}$ frames of data via sample averaging (SA) method. This detector can be considered the application of the well-known AMF detector in MIMO scenarios where clutter consists of multiple and extended scatterers and beam-squint effects are visible. This is why this kind of detector is denoted as "SA-AMF". In (16), instead of $\mathbf{R}_n^{\boldsymbol{\eta}}$, SA-AMF, $\mathcal{V}_1$ detector uses the estimated interference angle covariance matrix $\hat{\mathbf{R}}_n^{\boldsymbol{\eta}}$ which was learnt via SA method. Similar to Given $\mathbf{X}_n$, $\mathcal{V}_1$ detector, the $\boldsymbol{\omega}_n$ filters must be constructed N times per frame. However, if the beam-squint and Doppler mismatch are ignored, $\mathbf{R}_n^{\boldsymbol{\eta}}$ can be assumed to be the same for all subcarriers. Therefore, it might be sufficient to use all subcarriers to learn a single covariance matrix $\hat{\mathbf{R}}^{\boldsymbol{\eta}}$ and use it to construct a single MIMO filter $\boldsymbol{\omega}$. On the other hand, if the beam-squint is effective, the angular channel of interference would depend on the subcarrier frequency, and a subband approach could be used to ease the calculations.

The working principle of SA-AMF detectors with a subband approach is explained in more detail in Fig. 3. As seen in Fig. 3, SA-AMF detectors divide the spectrum into subbands to mitigate the effects of beam-squint. There are $N/N' = \mathcal{N}$ subcarriers in each of the N' subbands, where $\mathcal{N}$ can be selected so that the beam-squint effect is negligible inside the subbands [32]. $\mathcal{T}$ frames of observation are assumed to be taken before the IT is present. The SA-AMF, $\mathcal{V}_1$ detector uses these $\mathcal{T}$ frames and $\mathcal{N}$ subcarriers to estimate the angular interference covariance matrix $\hat{\mathbf{R}}_{n'}^{\boldsymbol{\eta}}$ of $(n')^{\text{th}}$ subband via SA. Then, the same $\boldsymbol{\omega}_{n'}$ is used for all $\mathcal{T}$ frames and $\mathcal{N}$ subcarriers in each subband. As the result of the angular processing, there are $\mathcal{T}$ vectors to be processed in range domain, t^{th} of them being denoted as $\mathbf{r}^{(t)}$. $\mathbf{D}^{\boldsymbol{\eta}}$ in Fig. 3 represents a diagonal load matrix, which guarantees that the matrix inversion converges. In this study, $\mathbf{D}^{\boldsymbol{\eta}}$ is proportional to expected noise angle covariance matrix, which is $\mathbf{D}^{\boldsymbol{\eta}} = \gamma_{load}\sigma_n^2 \operatorname{diag}\{\mathbf{I}_{D_t} \otimes (\mathbf{W}_r^H\mathbf{W}_r)\}$, where γ_{load} is the diagonal loading factor.

SA-AMF, $\mathcal{V}_1$ detector can be used when the angular information of UITs is not available at hand, but to be estimated. This detector is also compatible with subband processing, therefore it can learn the angular information of UITs in the scenarios with severe beam-squint effects.

4) KA-SARP Given $\mathbf{X}_n$, $\mathcal{V}_2$ detector: In this detector, the range filter $\mathbf{u}$ in (22) is constructed using the true knowledge of interference range covariance matrix $\mathbf{\Sigma}^{\boldsymbol{\eta}}$, provided by the

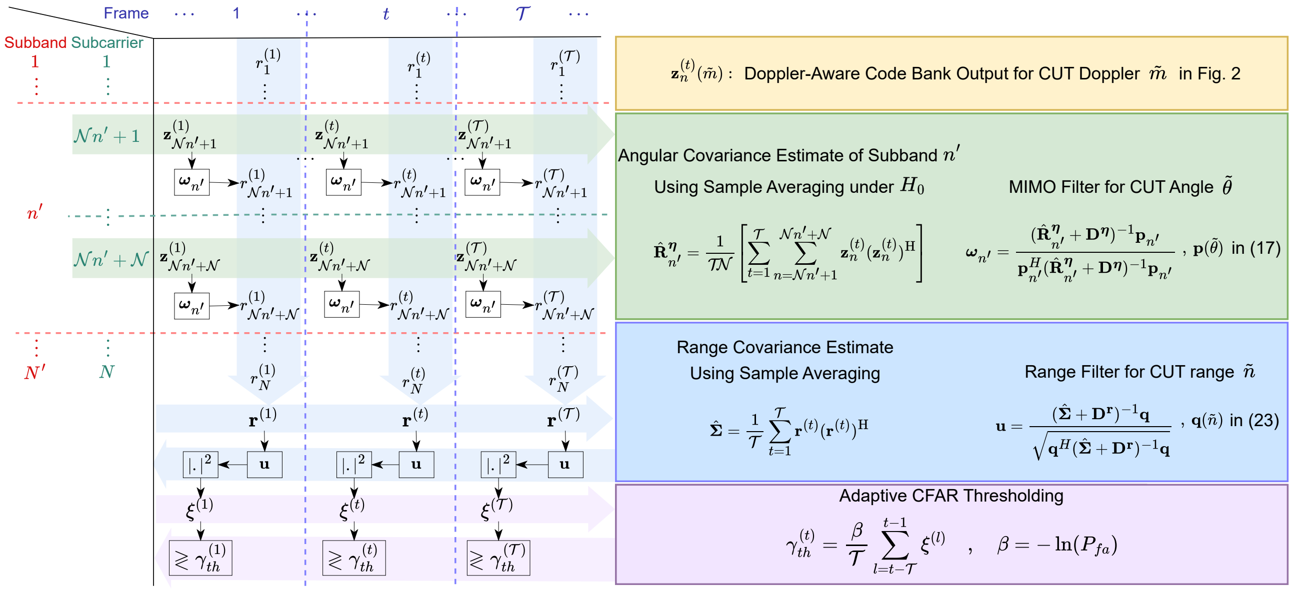

Fig. 3. Working principal and frame structure of the Fully-Adaptive (FA) Sample-Averaging (SA) detector, with a focus on subband approach

TABLE I
ALTERNATIVE FILTER TYPES FOR THE PROPOSED DETECTOR STRUCTURE

Name of processing method	MIMO Filter $\boldsymbol{\omega}_n$	Range Filter $\mathbf{u}$	Knowledge Required	Computational Complexity per CUT
Given $\mathbf{X}_n$, $\mathcal{V}_1$	$\boldsymbol{\omega}_n(\mathbf{R}_n^{\boldsymbol{\eta}})$	$\mathbf{u}(\mathbf{I}_N)$	$\mathbf{X}_n, \mathbf{D}_k^{\mathcal{C}}, \theta_k, \mathbf{R}_k^{\boldsymbol{\alpha}}$	$\mathcal{O}(\mathcal{K}NM^3D_t^2D_r\mathcal{T})$
Given $\mathbf{X}_n$, $\mathcal{V}_2$	$\boldsymbol{\omega}_n(\mathbf{I}_{D_rD_t})$	$\mathbf{u}(\boldsymbol{\Sigma}^{\boldsymbol{\eta}})$	$\mathbf{X}_n, \mathbf{D}_k^{\mathcal{C}}, \theta_k, \tau_k, \mathbf{R}_k^{\boldsymbol{\alpha}}$	$\mathcal{O}(\mathcal{K}N^2M^3D_t^4D_r^3\mathcal{T})$
Expected, $\mathcal{V}_1$	$\boldsymbol{\omega}_n(\overline{\mathbf{R}}_n^{\boldsymbol{\eta}})$	$\mathbf{u}(\mathbf{I}_N)$	$\mathbf{D}_k^{\mathcal{C}}, \theta_k, \mathbf{R}_k^{\boldsymbol{\alpha}}$	$\mathcal{O}(N'D_t^2D_r^2)$
Expected, $\mathcal{V}_2$	$\boldsymbol{\omega}_n(\mathbf{I}_{D_rD_t})$	$\mathbf{u}(\overline{\boldsymbol{\Sigma}}^{\boldsymbol{\eta}})$	$\mathbf{D}_k^{\mathcal{C}}, \theta_k, \tau_k, \mathbf{R}_k^{\boldsymbol{\alpha}}$	$\mathcal{O}(N^2)$
SA-AMF, $\mathcal{V}_1$	$\boldsymbol{\omega}_n(\hat{\mathbf{R}}_n^{\boldsymbol{\eta}})$	$\mathbf{u}(\mathbf{I}_N)$	—	$\mathcal{O}(\bar{N}D_t^2D_r^2\mathcal{T})$
SA-AMF, $\mathcal{V}_2$	$\boldsymbol{\omega}_n(\mathbf{I}_{D_rD_t})$	$\mathbf{u}(\hat{\boldsymbol{\Sigma}}^{\boldsymbol{\eta}})$	—	$\mathcal{O}(N^2\mathcal{T}+N^3)$
3D Perio	$\boldsymbol{\omega}_n(\mathbf{I}_{D_rD_t})$	$\mathbf{u}(\mathbf{I}_N)$	—	$\mathcal{O}(N'D_tD_r)$

tracker. As shown in (25), this range filter is dependent on Tx symbols $\mathbf{X}_n$, but there is only one matrix inversion of size $N \times N$ is required per frame. Therefore, this detector is computationally less burdensome than Given $\mathbf{X}_n$, $\mathcal{V}_1$ detector. This detector must be used only if both angular and range information of UITs are available and there is not a constraint on the computational power.

5) KA-SARP with Expected $\mathbf{X}_n$, $\mathcal{V}_2$ detector: This detector forms the max-SINR range filter $\mathbf{u}$ in (22) by using $\overline{\boldsymbol{\Sigma}}^{\boldsymbol{\eta}}$ instead of $\boldsymbol{\Sigma}^{\boldsymbol{\eta}}$. Similar to Expected $\mathbf{X}_n$, $\mathcal{V}_1$ detector, the filters can be calculated only once in several frames because the range response of the scatterers is assumed to stay correlated for several OFDM frame durations. This detector can be used when both angular and range information of UITs are available but there is only a limited computational power.

6) Fully Adaptive AMF-like SARP with SA, $\mathcal{V}_2$ detector: In (22), instead of $\boldsymbol{\Sigma}^{\boldsymbol{\eta}}$, SA-AMF, $\mathcal{V}_2$ detector uses the estimated interference range covariance matrix $\hat{\boldsymbol{\Sigma}}^{\boldsymbol{\eta}}$ which was learnt via SA method. As shown in Fig. 3, $\hat{\boldsymbol{\Sigma}}^{\boldsymbol{\eta}}$ is learned in each frame, and then the average of these matrices is used to create the range filter $\mathbf{u}$ to be used in all $\mathcal{T}$ frames. $\mathbf{D}^{\mathbf{r}}$ in Fig. 3 represents a diagonal load matrix, which guarantees that the matrix inversion converges. In this study, $\mathbf{D}^{\mathbf{r}}$ is proportional to the expected noise range covariance matrix, whose $(n,n)^{\text{th}}$ element is $[\mathbf{D}^{\mathbf{r}}]_{(n,n)} = \gamma_{load}\sigma_n^2||\mathbf{W}_t^H\mathbf{b}_n(\tilde{\theta})||^2||\mathbf{W}_r\mathbf{W}_r^H\mathbf{a}_n(\tilde{\theta})||^2$, where γ_{load} is the diagonal loading factor.

As explained in (27), Doppler mismatch results in $\boldsymbol{\Sigma}^{\boldsymbol{\eta}}$ being dependent on $\mathbf{X}_n$. This dependence can be described as element-wise multiplication with a random matrix $\mathbf{A}_k$, which is zero-mean when the expectation is taken over $\mathbf{X}_n$. To estimate the deterministic part in $\boldsymbol{\Sigma}^{\boldsymbol{\eta}}$, which is $\mathbf{q}_k^{\mathcal{C}}(\mathbf{q}_k^{\mathcal{C}})^H$ in (27), the same $\mathbf{X}_n$ matrix must be repeated for multiple frames to prevent the range information from being nullified. Therefore, $\mathbf{X}_n$ symbols are repeated frame-to-frame in this paper, which has an adverse effect on the communication rate. However, it should be noted that the repetition occurs only in N subcarriers among all N' subcarriers; and after the training period is finished, the range filters of SA-AMF, $\mathcal{V}_2$ detector can be fixed and the communication rate can be recovered. [5] SA-AMF, $\mathcal{V}_2$ detector can be used when the range information

[5]The training of SA-AMF filters is done under H_0 hypothesis in this study. However, it can also be done under H_1 hypothesis without losing SINR by using an increased number of training symbols.

of UITs is not available at hand, but to be estimated with a slight decrease in the communication rate.

It should be noted that as the training goes to infinity, SA-AMF, $\mathcal{V}_1$ detector approaches Expected $\mathbf{X}_n$, $\mathcal{V}_1$ detector, and SA-AMF, $\mathcal{V}_2$ detector approaches Given $\mathbf{X}_n$, $\mathcal{V}_2$ detector. This is because in SA-AMF, $\mathcal{V}_1$, different $\mathbf{X}_n$ sequences are used in training, effectively averaging the MIMO filters over $\mathbf{X}_n$. On the other hand, in SA-AMF, $\mathcal{V}_2$, the same $\mathbf{X}_n$ is repeated so that the range covariance is learned as if $\mathbf{X}_n$ is given.

7) 3-D Periodogram detector: As a benchmark detector, we also utilize 3-D periodogram, which is a nonparametric method commonly used in the literature, as in [15], [37]. This detector uses no knowledge of interference and performs conventional DFT or IDFT in range, angle and Doppler domains. This detector is used if the computational power is severely limited.

The calculation of filters for different processing methods, along with the required knowledge and computational complexities of them, are summarized in Table I. For the computational complexities, the most complex operation that is done for each frame is considered for each method. Given $\mathbf{X}_n$ methods must calculate the true covariances for each frame. Therefore, they are by far the most complex methods.

B. *The Effects of Beam-Squint on Different Filter Types*

When f_c/W ratio of the system is significantly low, beam-squint effects become non-negligible. A discussion on how large the bandwidth of the system can be while keeping the beam-squint effect small is provided in [32], and is not in the scope of this study. The beam-squint directly affects the receive and transmit steering vectors, $\mathbf{a}_n$ and $\mathbf{b}_n$, making them dependent on the subcarrier index n. Consequently, the angular covariance matrix, $\mathbf{R}_n^{\boldsymbol{\eta}}$ in (19), and the angular steering vector towards the IT, $\mathbf{p}_n$ in (17), are directly affected by beam-squint. The steering vectors $\mathbf{p}_n$ can be easily calculated once for each subcarrier, therefore it does not bring additional computational complexity to the system. However, $\mathbf{R}_n^{\boldsymbol{\eta}}$ depends on the transmitted symbols $\mathbf{X}_n$ and should be calculated for each transmitted OFDM symbol. On the other hand, to calculate the angular filter $\boldsymbol{\omega}_n$, the inverse of the $\mathbf{R}_n^{\boldsymbol{\eta}}$ matrix must be taken for each OFDM symbol, requiring a large computational power. Therefore, we proposed different filter types that ease the $\mathbf{R}_n^{\boldsymbol{\eta}}$ calculations, effectively having different behaviors against beam-squint. In this section, these behaviors will be briefly discussed for three different implementations of $\mathcal{V}_1$ detector, as they are the only ones which use $\mathbf{R}_n^{\boldsymbol{\eta}}$ information.

1) KA-SARP Given $\mathbf{X}_n$, $\mathcal{V}_1$ detector: As explained in Section IV-A1, this filter type calculates the covariance matrix $\mathbf{R}_n^{\boldsymbol{\eta}}$ for every subcarrier. Therefore, it can mitigate the effects of beam-squint inherently, using a high computational power. On the other hand, the covariance matrix can be calculated for only N' number of subbands to ease the calculations. As the f_c/W ratio decreases, the number of subbands required to keep the performance loss at minimum increases. If this filter is used with fewer subbands than required, it can suffer from performance losses due to beam-squint because it selectively suppresses the clutter in angular domain. Therefore, this filter must be used with enough number of subbands to get the optimal interference suppression in angular domain.

2) Expected $\mathbf{X}_n$, $\mathcal{V}_1$ detector: As explained in Section IV-A2, this filter type calculates only one covariance matrix for the sake of ease of calculations. Therefore, its performance would be negatively affected by the beam-squint. The subband approach can also be used with this filter to mitigate the beam-squint effects; the expected covariance matrices can be calculated for each of the N' subbands, taking the expectations over the corresponding $\mathcal{N}$ subcarriers in the subbands.

3) Fully Adaptive AMF-like SARP with SA, $\mathcal{V}_1$ detector: As explained in Section IV-A3, this filter type estimates the covariance matrices for each of the N' subband, training over the corresponding $\mathcal{N}$ subcarriers in the subbands. However, since $\bar{N}$ subcarriers are used for communication purposes, the training of SA-AMF, $\mathcal{V}_1$ detector can be done using all $\bar{N}$ subcarriers to increase the estimation accuracy. This filter suffers from beam-squint if N' is selected smaller than needed, but increasing N' might result in reduction in estimation accuracy of $\mathbf{R}_{n'}^{\boldsymbol{\eta}}$, indicating a trade-off.

V. Numerical Evaluations

In this section, the proposed and benchmark detectors are numerically evaluated. First, the simulation parameters are provided and their effects on output SINR are discussed. Then, two beamforming schemes investigated in this study are explained. Finally, the simulation results are given for the cases when beam-squint effect is small and severe.

A. *Simulation Parameters*

The simulation parameters are provided in Table II. In Table II, (BS) represents the cases where beam-squint effect is severe, which is satisfied by increasing the actual number of subcarriers, $\bar{N}$, 16 times while keeping the number of subcarriers for radar signal processing, N, the same. Therefore, effectively, Δf is increased and range resolution is decreased 16 times in the BS simulations. There are $\mathcal{K} = 10$ UIT scatterers and $\mathcal{U} = 2$ UL users. The first UIT is assumed to be a single scatterer with $r_1 = 0$ m, $v_1 = 0$ m/s, $\sigma_k^{\mathcal{C}} = 0$ Hz and $\gamma_k^{\mathcal{C}} = 30$ dB, depicting a strong self-interference. The other UIT scatterers are in a cluster, which depicts an object of finite and nonzero length and width. The center range is 18.11 m (10^{th} range bin) and the center angle is -12 degrees for this object. The length and width of the object are half of the range and angle resolutions of the system, respectively. We consider that the scattering points are on the edge centers and corners of the object in both range and angle dimensions, as well as the center of it, resulting in 9 scattering points. The velocity, Doppler spread and total reflected power from the object are 20 m/s (0.63^{th} Doppler bin), 200 Hz and 20 dB, respectively. The UL users are at 7.5 and 12.5 degrees, and the average received powers from them are 10 dB each. The UL users are assumed to have no velocity or Doppler spread, and they are not considered as separate scattering objects for the sake of simplicity. To ease the understanding of the graphs, red dashed and blue dash-dotted vertical lines are drawn wherever the UITs and SoIs are located, respectively.

It should be noted that the output SINR metric corresponds to the SINR improvement factor in our simulations because

TABLE II
SIMULATION PARAMETERS

Parameter	Meaning	Value	Parameter	Meaning	Value
$\bar{N}$	total # of subcarriers	1024	N	# of ISAC subcarriers	32
M	# of OFDM symbols	16	$\mathcal{T}$	# of frames	16
N'	# of subbands	32	N' (BS)	# of subbands for BS case	8, 1
$\mathcal{N}$	# of subcarriers in each subband	1	$\mathcal{N}(BS)$	# of subcarriers in each subband for BS case	4, 32
N_t, N_r	# of Tx, Rx antennas	64	D_t, D_r	# of Tx, Rx RF chains	10
T_s	OFDM symbol duration	12.38 μs	T_f	frame duration	198 μs
$\Delta f = W/N$	subcarrier spacing	2.59 MHz	W	bandwidth	82.75 MHz
Δf (BS)	subcarrier spacing for BS case	41.37 MHz	W (BS)	bandwidth for BS case	1.32 GHz
f_c	center frequency	24 GHz	λ_c	center wavelength	12.5 mm
c	speed of light in vacuum	2.998×10^8 m/s	$\gamma_0^{\mathcal{C}}/\sigma_n^2$	target power	1 (0 dB)
$\gamma_k^{\mathcal{C}}/\sigma_n^2$	clutter power	30, 20 dB	$\gamma_u^{\mathcal{S}}/\sigma_n^2$	SoI power	10 dB
γ_{load}	diagonal loading factor	3	NMN_rN_t/D_t	maximum processing gain	53.22 dB

the IT power is selected to be unity. Each parameter has different effects on the SINR improvement factor. For example, by increasing the number of antenna elements, the SINR improvement factor, the angular resolution and angular interference suppression capabilities can be improved, with a higher computational cost. Increasing M while keeping T_s the same would improve the SINR improvement factor and Doppler resolution, but the channel correlation time would be a limitation on M. Increasing N would result in different types of effects. In this study, we focus on a communication system that uses $\bar{N}$ subcarriers, while N of them are utilized for sensing purposes in ISAC. We assume that the N subcarriers are selected to cover the whole bandwidth W with uniform spacing. Within this configuration, increasing N while keeping $\bar{N}$ the same would result in an increase in SINR improvement factor and the maximum unambiguous range, and additional interference suppression in range domain. On the other hand, increasing N while keeping Δf the same would result in an improvement in range resolution.

B. Beamforming Scenarios

Two different beamforming schemes are simulated in this study. In the first scenario, both Tx and Rx beams are formed to cover the angle interval of $(-7.5, 7.5)$ degrees, which is called as *fully overlapping (FO) scheme*. In the second scenario, Tx beamformer covers the angle interval of $(-20, -5)$ degrees and Rx beamformer covers the angle interval of $(5, 20)$ degrees, which is called as *no overlapping (NO) scheme*. The Tx and Rx beamforming gain patterns, and their multiplication depicting the total beamforming gain pattern, are provided in Fig. 4. Tx and Rx beamforming gain pattern values at the n^{th} subcarrier for angle θ is equal to $\text{Tr}\{\mathbf{a}_n(\theta)^H \mathbf{W}_t \mathbf{W}_t^H \mathbf{a}_n(\theta)/M\}$ and $\text{Tr}\{\mathbf{b}_n(\theta)^H \mathbf{W}_r \mathbf{W}_r^H \mathbf{b}_n(\theta)\}$, respectively. It should be noted that the gain is N_t/D_t inside the flat Tx sector because a total Tx power constraint is assumed. On the other hand, the whole N_r beamforming gain is achieved on the receiver side.

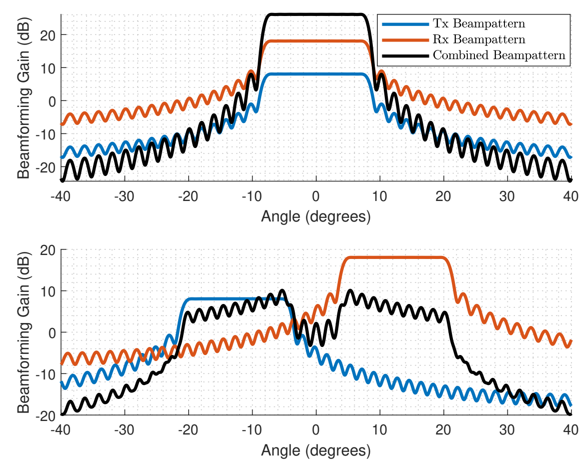

Fig. 4. Tx, Rx and combined antenna gain patterns for fully overlapping (top) and no overlapping (bottom) schemes

C. Simulation Results

In this section, output SINR values for five different detectors will be given for different values of CUT angle, range and Doppler bins. In addition, P_d vs input SNR curves for two different CUT locations are also provided for these detectors. The first detector uses 'Given $\mathbf{X}_n$' processing for both $\mathcal{V}_1$ and $\mathcal{V}_2$, and it is labeled as '$\mathcal{V}_1$&$\mathcal{V}_2$ Given $\mathbf{X}_n$' in the legends. Since this detector uses $\mathbf{X}_n$ data for both variants, its SINR is expected to be the upper limit for all other detectors. The second detector uses 'Expected $\mathbf{X}_n$' processing for both $\mathcal{V}_1$ and $\mathcal{V}_2$, and it is labeled as '$\mathcal{V}_1$&$\mathcal{V}_2$ Expected $\mathbf{X}_n$' in the legends. Since this detector does not use $\mathbf{X}_n$ data for any variants, it is expected to suffer from the Doppler mismatch effect mentioned before, but its filters must be calculated only once per several frames. The third detector uses 'Expected $\mathbf{X}_n$' processing for $\mathcal{V}_1$ but 'Given $\mathbf{X}_n$'processing for $\mathcal{V}_2$, and it is labeled as '$\mathcal{V}_1$ Expected $\mathbf{X}_n$&$\mathcal{V}_2$ Given $\mathbf{X}_n$' in the legends. This detector does require $\mathbf{X}_n$ data for range processing but uses expected filters for angle processing. Since

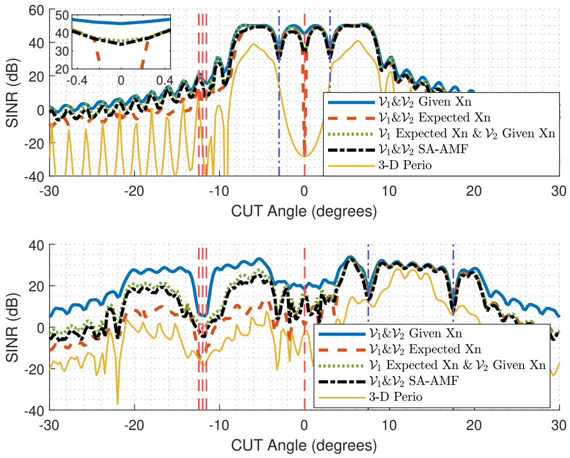

Fig. 5. SINR vs CUT angle graphs for fully-overlapping (top) and non-overlapping (bottom) scenarios, CUT Range bin: 0 (top) and 10 (bottom), CUT Doppler bin: 0.32 (10 m/s)

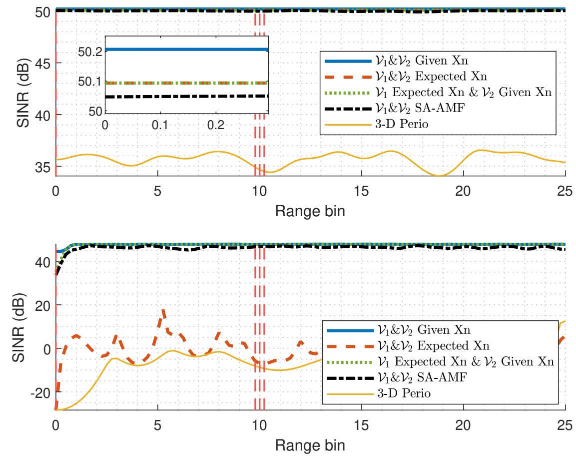

Fig. 6. SINR vs CUT range bin graphs for FO scenario, CUT Angle: 5 degrees (top) and 0 degrees (bottom), CUT Doppler bin: 0.32 (10 m/s)

the Doppler mismatch effect is more severe in range rather than angle processing, this detector is expected to overcome this difficulty while its complexity is reduced with respect to the '$\mathcal{V}_1\&\mathcal{V}_2$ Given $\mathbf{X}_n$' detector. The fourth detector uses 'SA-AMF' processing for both $\mathcal{V}_1$ and $\mathcal{V}_2$, and it is labeled as '$\mathcal{V}_1\&\mathcal{V}_2$ SA-AMF' in the legends. This detector adaptively learns both angle and range covariance matrices. Since its learning inherently includes the effects of $\mathbf{X}_n$, this detector is expected to overcome the Doppler mismatch problem, and its MIMO filters can be calculated only once after the training period of several frames. The last detector uses 'conventional DFT,' or '3-dimensional periodogram' processing for both $\mathcal{V}_1$ and $\mathcal{V}_2$, and it is labeled as '3-D Perio' in the legends. This detector does not use any information about the interference or $\mathbf{X}_n$ and is expected to perform the worst among others in general. For DFT and IDFT processings in angle and range domains, windowing is applied conventionally [42]. Therefore in this study, Chebyshev windows are used with sidelobe suppression values of 50 dB and 100 dB, respectively. Since all detectors use conventional DFT or IDFT processing at one of their variants, they suffer from a windowing loss of around 3.2 dB. The detectors other than 3-D Perio can bypass windowing without losing sidelobe performances, but we kept the windows in the simulations for the sake of fairness.

1) Beam-squint effect is small: SINR vs CUT angle graphs for two different scenarios are provided in Fig. 5. The top graph in Fig. 5 represents a FO case where both a UIT and two SoIs are inside the overlapping Tx-Rx sectors. It is seen that all detectors except 3-D Perio perform similarly when the CUT angle is away from UITs or SoIs. However, when CUT is on top of the UIT in both angle and range, $\mathcal{V}_1\&\mathcal{V}_2$ Expected $\mathbf{X}_n$ and 3-D Perio detectors fail to suppress the interference while other detectors can. This region is where the only difference between the IT and the UIT is in Doppler domain. However, as explained before, $\mathbf{X}_n$ knowledge is required to suppress the interference using the Doppler diversity. Therefore, the detectors that know (or learn) $\mathbf{X}_n$ information can suppress the UIT while other detectors fail to reach a high SINR. An important aspect of the clutter suppression here is that all detectors use the same Doppler preprocessing. However, the Doppler mismatch shows itself in both angle and range covariance matrices, and the clutter can be suppressed in Doppler domain with MIMO and range processing. The only difference between $\mathcal{V}_1\&\mathcal{V}_2$ Expected $\mathbf{X}_n$ and $\mathcal{V}_1$ Expected $\mathbf{X}_n\&\mathcal{V}_2$ Given $\mathbf{X}_n$ detectors is the range processing part, but the SINR difference is more than 60 dB between them at CUT angle 0 degree. Similarly, the only difference between $\mathcal{V}_1$ Expected $\mathbf{X}_n\&\mathcal{V}_2$ Given $\mathbf{X}_n$ and $\mathcal{V}_1\&\mathcal{V}_2$ Given $\mathbf{X}_n$ detectors is the MIMO processing part, and the SINR difference is around 10 dB between them at CUT angle 0 degree. This shows that Doppler mismatch effect is more severe in the range rather than the angle processing. The bottom graph in Fig. 5 represents a NO case, where Tx and Rx sectors are separated. It can be seen that the importance of good MIMO processing is more visible when the sectors are separated. When the CUT angle is near (but not on top of) the UIT, $\mathcal{V}_1\&\mathcal{V}_2$ Given $\mathbf{X}_n$ detector can outperform the closest detector by around 7 dB. The effects of Doppler mismatch on both range and angle processings are still visible in this case.

SINR vs CUT range bin graphs for FO and NO scenarios are provided in Fig. 6 and Fig. 7, respectively. Similar to the case in Fig. 5, when the CUT angle is away from the interference, all detectors except 3-D Perio perform similarly, and when the CUT is on top of the interference, using $\mathbf{X}_n$ knowledge is important. In Fig. 7, it is seen that $\mathcal{V}_1\&\mathcal{V}_2$ Given $\mathbf{X}_n$ and $\mathcal{V}_1$ Expected $\mathbf{X}_n\&\mathcal{V}_2$ Given $\mathbf{X}_n$ detectors perform the same for most CUT ranges, only except on top of the UIT range. This shows that $\mathcal{V}_1$ variant performs better than $\mathcal{V}_2$ variant only when the CUT range is so close to UIT range. This is expected because $\mathcal{V}_1$ uses max-SINR MIMO processing and $\mathcal{V}_2$ uses max-SINR range processing. Fig. 7 shows that this 2-variant detector scheme benefits the scenarios where the interference can only be suppressed in one dimension.

To evaluate the effects of the number of ISAC subcarriers N on range processing performance, SINR vs CUT range bin

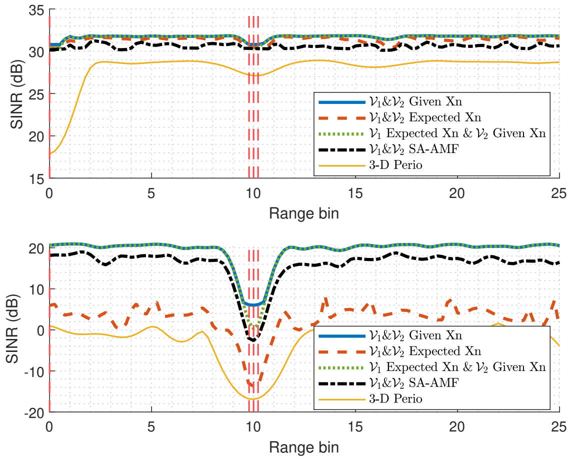

Fig. 7. SINR vs CUT range bin graphs for NO scenario, CUT Angle: 12 degrees (top) and -12.5 degrees (bottom), CUT Doppler bin: 0.32 (10 m/s)

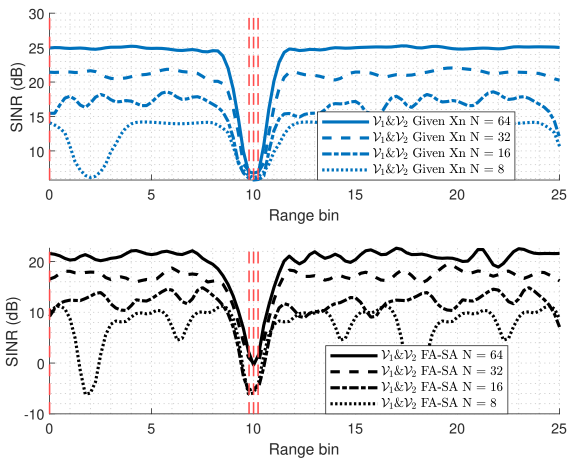

Fig. 8. SINR vs CUT range bin graphs for $\mathcal{V}_1\&\mathcal{V}_2$ Given $\mathbf{X}_n$ (top) and $\mathcal{V}_1\&\mathcal{V}_2$ SA-AMF (bottom) detectors in a NO scenario, CUT Angle: -12.5 degrees, CUT Doppler bin: 0.32 (10 m/s)

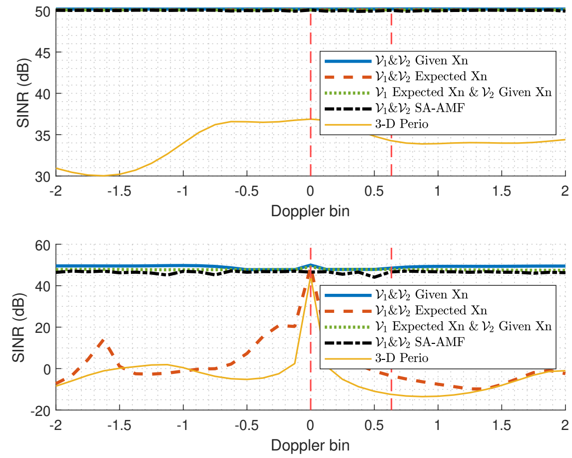

Fig. 9. SINR vs CUT Doppler bin graphs for FO scenario, CUT Angle: 5 degree (top) and 0 degree (bottom), CUT Range bin: 10

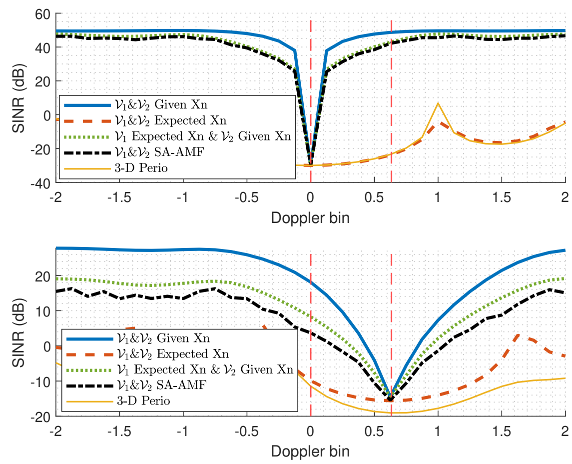

Fig. 10. SINR vs CUT Doppler bin graphs for FO (top) and NO (bottom) scenarios, CUT Angle: 0 degrees (top) and -12 degrees (bottom), CUT Range bin: 0 (top) and 10 (bottom)

graphs in a NO scenario for different N values are provided in Fig. 8. In Fig. 8, N value is changed while $\bar{N}$ is kept the same, meaning that the total bandwidth and range resolution remained constant. It can be seen that both $\mathcal{V}_1\&\mathcal{V}_2$ Given $\mathbf{X}_n$ and $\mathcal{V}_1\&\mathcal{V}_2$ SA-AMF detectors can suppress the interference in range domain when the IT and the UITs are separated enough. The SINR difference between the two methods is due to the limited training data of SA-AMF detector ($\mathcal{T} = 16$ frames). The SINR differences between consecutive N selections are roughly 3 dB, as expected. On the other hand, as the dimensions of $\mathbf{\Sigma}^{\eta}$ increases, interference suppression capabilities in range domain also increase, resulting in a smoother SINR response. It should be noted that when $N = 8$, the maximum unambiguous range is decreased so much that the range response is seen as folded in Fig. 8. It can also be seen that $N = 32$ selection is a useful compromise between interference suppression capabilities and computational complexity.

SINR vs CUT Doppler bin graphs for two different CUT angles for a FO scenario are provided in Fig. 9. In the top graph of Fig. 9, all detectors except 3-D Perio perform similarly as in the other graphs before. In the bottom graph of Fig. 9, it is seen that when the suppression in angle domain is impossible, the suppression in the range domain depends on the CUT Doppler. When the CUT Doppler is the same as the UIT Doppler, range processing can successfully suppress the clutter for all detectors. However, when there is Doppler mismatch, the detectors that do not use $\mathbf{X}_n$ information fail to suppress the UIT even if it is separated in range domain. This clearly shows that Doppler mismatch can harm range processing if $\mathbf{X}_n$ information is not exploited.

SINR vs CUT Doppler bin graphs for the scenarios in which CUT angle and range bins are on top of UITs are provided in Fig. 10. When the CUT is on top of any UIT in both angle and range domains, the UIT can be suppressed only in Doppler domain. Therefore, the detectors using $\mathbf{X}_n$ information outperform the others when the CUT Doppler

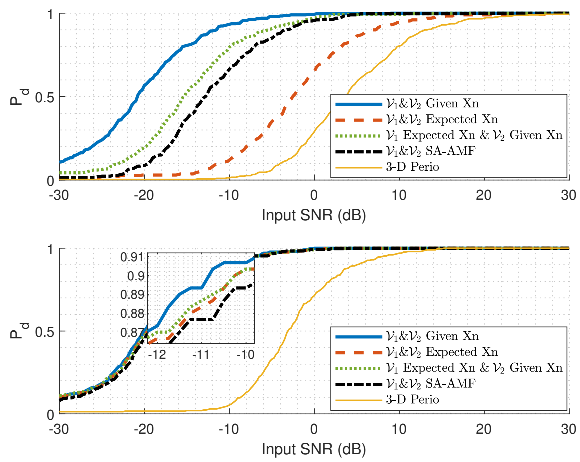

Fig. 11. P_d vs input SNR curves for NO scenarios, $P_{fa} = 10^{-3}$, number of Monte-Carlo trials: 300, CUT Range bin: 10, CUT Doppler bin: 0.32 (10 m/s), CUT Angle: -6 degree (top) and 16 degrees (bottom)

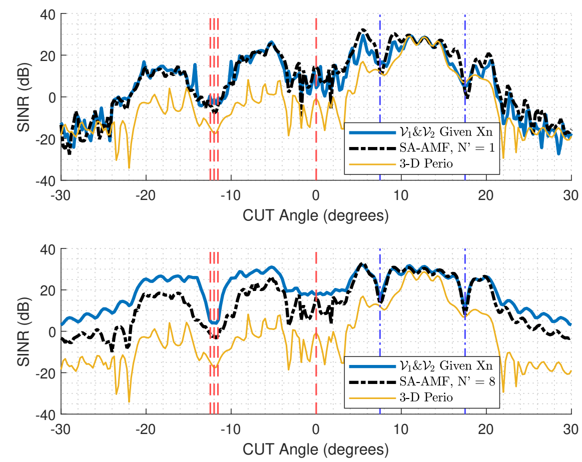

Fig. 12. SINR vs CUT angle graphs for NO scenarios when beam-squint effect is severe, CUT Range bin: 10, CUT Doppler bin: 0.32 (10 m/s). $f_c/W = 18.1274$. Number of subbands: 1 (top) and 8 (bottom)

is separated from the UIT Doppler. It can also be seen that Doppler spread of the UIT is also important and determines how much separation in Doppler is needed to create diversity and suppress the UIT.

P_d vs input SNR curves for two different CUT locations are provided in Fig. 11. In this figure, input SNR means the SNR value per subcarrier per antenna per symbol. For each detector, the CFAR threshold is determined by the formula $\gamma_{th} = -\ln(P_{fa}) * \beta$ where β is the detection metric at the detector input when H_0 hypothesis is true. Theoretically, this metric is equal to the denominator of the SINR expression in (30) for each detector. Since the covariance matrix and the filters in the expression depend on $\mathbf{X}_n$, the theoretic threshold also depends on $\mathbf{X}_n$. However, for successful detectors, interference is suppressed so that the $\mathbf{X}_n$ dependence of the thresholds is weak. On the other hand, adaptive CFAR thresholding using multiple training frames with different $\mathbf{X}_n$ data can also be used to average out the effects of $\mathbf{X}_n$ on the thresholds. A similar adaptive thresholding method is explained in [34]. In Fig. 11, average thresholds are found for $P_{fa} = 10^{-3}$ and 300 Monte-Carlo trials are conducted to find P_d values. It can be seen in Fig. 11 that P_d vs input SNR curves give similar results to SINR curves, as expected.

2) Beam-squint effect is severe: The beam-squint effect when f_c/W ratio is relatively small is investigated in Fig. 12. In the top graph of Fig. 12, the detectors do not care about the beam-squint effect and use only a single subband, applying the same angular processing for all subcarriers. It can be seen that the performance of the detectors decreases due to the misinformation on MIMO processing caused by the beam-squint effect. On the other hand, $\mathcal{V}_1\&\mathcal{V}_2$ Given $\mathbf{X}_n$ detector tries to put a sharp null on a wrong angle and therefore its SINR cannot be interpreted as an upper limit to other detectors anymore. Besides this, SA-AMF detector learns the angle information from all subcarriers, which all have different angle information due to the beam-squint effect, and therefore tries to nullify a wider set of angles than it should be.

When the bottom graph of Fig. 12 is investigated, it can be seen that subband approach can be used to mitigate the negative effects of beam-squint. When $N' = 8$, the MIMO processing filters consider different amounts of suppression for 8 different angles, therefore the UIT can be suppressed better for both detectors. The performance increase in $\mathcal{V}_1\&\mathcal{V}_2$ Given $\mathbf{X}_n$ detector is around 10 dB for some angles, showing that subband approach is a valid method to mitigate the negative effects of beam-squint and make full use of the UIT covariance information while keeping the computational complexity lower than the case when $N' = 32$.

It can be inferred from Fig. 12 that beam-squint effect can be detrimental if it is not taken into account and the same filter is used for all subcarriers. However, it is not necessary to always use different filters for all subcarriers, a subband approach can be enough depending on the severity of beam-squint effect. It can also be seen in Fig. 12 that our proposed KA-SARP filters outperform others by suppressing the interference even if it spreads angularly due to the beam-squint effect.

VI. Conclusion

This paper proposed a radar detector structure for a MIMO-OFDM ISAC system under the disruptive effects of Doppler mismatch, beam-squint, UL users and multiple scatterers in fractional Doppler-angle-range bins. The introduction of the DACB and coupling between Doppler mismatch and Tx symbols was crucial in understanding the nature of the MIMO-OFDM ISAC systems. The sub-optimal SARP method proved effective in maximizing the output SINR, with the help of a novel two-variant detector scheme. On the other hand, the possible beam-squint effect dictated that MIMO processing should be done before range processing in SARP. The proposed subband approach effectively addressed the beam-squint effect. Simulation results confirmed the superior performance of our proposed detectors compared to conventional methods, highlighting their potential in enhancing MIMO ISAC system performance for 6G systems.

REFERENCES

[1] L. G. De Oliveira, B. Nuss, M. B. Alabd, A. Diewald, M. Pauli, and T. Zwick, “Joint Radar-Communication Systems: Modulation Schemes and System Design,” *IEEE Trans. Microw. Theory Techn.*, vol. 70, no. 3, pp. 1521–1551, 3 2022.

[2] F. Liu, Y. Cui, C. Masouros, J. Xu, T. X. Han, Y. C. Eldar, and S. Buzzi, “Integrated Sensing and Communications: Toward Dual-Functional Wireless Networks for 6G and Beyond,” *IEEE J. Sel. Areas Commun.*, vol. 40, no. 6, pp. 1728–1767, 6 2022.

[3] J. A. Zhang, F. Liu, C. Masouros, R. W. Heath, Z. Feng, L. Zheng, and A. Petropulu, “An Overview of Signal Processing Techniques for Joint Communication and Radar Sensing,” *IEEE J. Sel. Topics Signal Process.*, vol. 15, no. 6, pp. 1295–1315, 2021.

[4] C. B. Barneto, S. D. Liyanaarachchi, M. Heino, T. Riihonen, and M. Valkama, “Full Duplex Radio/Radar Technology: The Enabler for Advanced Joint Communication and Sensing,” *IEEE Wirel. Commun.*, vol. 28, no. 1, pp. 82–88, 2021.

[5] N. González-Prelcic, M. Furkan Keskin, O. Kaltiokallio, M. Valkama, D. Dardari, X. Shen, Y. Shen, M. Bayraktar, and H. Wymeersch, “The Integrated Sensing and Communication Revolution for 6G: Vision, Techniques, and Applications,” *Proceedings of the IEEE*, vol. 112, no. 7, pp. 676–723, 2024.

[6] X.-Y. Wang, S. Yang, J. Zhang, C. Masouros, and P. Zhang, “Clutter Suppression, Time-Frequency Synchronization, and Sensing Parameter Association in Asynchronous Perceptive Vehicular Networks,” *IEEE J. Sel. Areas Commun.*, vol. 42, no. 10, pp. 2719–2736, 2024.

[7] X.-Y. Wang, S. Yang, H.-Y. Zhai, C. Masouros, and J. A. Zhang, “Windowing optimization for fingerprint-spectrum-based passive sensing in perceptive mobile networks,” *IEEE Trans. Commun.*, 2024.

[8] W. Jiang, Z. Wei, S. Yang, Z. Feng, and P. Zhang, “Cooperation-Based Joint Active and Passive Sensing With Asynchronous Transceivers for Perceptive Mobile Networks,” *IEEE Trans. Wireless Commun.*, vol. 23, no. 10, pp. 15 627–15 641, 2024.

[9] S. D. Liyanaarachchi, T. Riihonen, C. B. Barneto, and M. Valkama, “Joint MIMO Communications and Sensing With Hybrid Beamforming Architecture and OFDM Waveform Optimization,” *IEEE Trans. Wireless Commun.*, vol. 23, no. 2, pp. 1565–1580, 2024.

[10] K. M. Braun, “OFDM Radar Algorithms in Mobile Communication Networks,” Ph.D. dissertation, Karlsruhe, Karlsruher Institut für Technologie (KIT), Diss., 2014, 2014.

[11] S. D. Liyanaarachchi, T. Riihonen, C. B. Barneto, and M. Valkama, “Optimized Waveforms for 5G-6G Communication with Sensing: Theory, Simulations and Experiments,” *IEEE Trans. Wireless Commun.*, vol. 20, no. 12, pp. 8301–8315, 12 2021.

[12] N. M. Idrees, Z. Lu, M. Saqlain, H. Zhang, S. Wang, L. Zhang, and X. Yu, “A W-Band Communication and Sensing Convergence System Enabled by Single OFDM Waveform,” *Micromachines*, vol. 13, no. 2, p. 312, 2022.

[13] C. B. Barneto, S. D. Liyanaarachchi, T. Riihonen, M. Heino, L. Anttila, and M. Valkama, “Beamforming and Waveform Optimization for OFDM-based Joint Communications and Sensing at mm-Waves,” in *Proc. 54th Asilomar Conf. Signals Syst. Comput.*, 2020, pp. 895–899.

[14] M. Temiz, E. Alsusa, and L. Danoon, “A Receiver Architecture for Dual-Functional Massive MIMO OFDM RadCom Systems,” in *Proc. IEEE Int. Conf. Commun. Workshops*. IEEE, 2020, pp. 1–6.

[15] M. Temiz, E. Alsusa, and M. W. Baidas, “A Dual-Functional Massive MIMO OFDM Communication and Radar Transmitter Architecture,” *IEEE Trans. Veh. Technol.*, vol. 69, no. 12, pp. 14 974–14 988, 2020.

[16] C. B. Barneto, T. Riihonen, M. Turunen, L. Anttila, M. Fleischer, K. Stadius, J. Ryynänen, and M. Valkama, “Full-Duplex OFDM Radar with LTE and 5G NR Waveforms: Challenges, Solutions, and Measurements,” *IEEE Trans. Microw. Theory Techn.*, vol. 67, no. 10, pp. 4042–4054, 2019.

[17] Y. Lai, M. F. Keskin, H. Wymeersch, L. Venturino, W. Yi, and L. Kong, “Subspace-Based Detection in OFDM ISAC Systems Under Different Constellations,” in *ICASSP 2024*, 2024, pp. 9126–9130.

[18] B. Kong, Y. Wang, X. Deng, and D. Qin, “Joint Range-Doppler-Angle Estimation for OFDM-Based RadCom System via Tensor Decomposition,” *Wirel. Commun. Mob. Comput.*, vol. 2018, pp. 1–12, 08 2018.

[19] Y. Huang, S. Hu, S. Ma, Z. Liu, and M. Xiao, “Designing Low-PAPR Waveform for OFDM-Based RadCom Systems,” *IEEE Trans. Wireless Commun.*, vol. 21, no. 9, pp. 6979–6993, 2022.

[20] L. Pucci, E. Matricardi, E. Paolini, W. Xu, and A. Giorgetti, “Performance Analysis of Joint Sensing and Communication based on 5G New Radio,” in *2021 IEEE GC Wkshps*. IEEE, 2021, pp. 1–6.

[21] S. D. Liyanaarachchi, C. B. Barneto, T. Riihonen, M. Heino, and M. Valkama, “Range–Angle Processing for Target Detection in Joint MIMO-OFDM Communications and Sensing,” in *Proc. IEEE SPAWC*. IEEE, 2021, pp. 486–490.

[22] Z. Wan, Z. Gao, S. Tan, and L. Fang, “Joint Channel Estimation and Radar Sensing for UAV Networks with mmWave Massive MIMO,” in *Proc. Int. Wireless Commun. Mobile Comput. (IWCMC)*, 2022, pp. 44–49.

[23] Q. Yang, H. Wu, Q. Huang, J. Zhang, H. Chen, W. Li, X. Tao, and Q. Zhang, “Side-lobe Can Know More: Towards Simultaneous Communication and Sensing for mmWave,” *Proc. ACM Interact. Mob. Wearable Ubiquitous Technol.*, vol. 6, no. 4, jan 2023. [Online]. Available: https://doi.org/10.1145/3569498

[24] S. Buzzi, C. D’Andrea, and M. Lops, “Using Massive MIMO Arrays for Joint Communication and Sensing,” in *Proc. 53rd Asilomar Conf. Signals Syst. Comput.* IEEE, 2019, pp. 5–9.

[25] M. F. Keskin, H. Wymeersch, and V. Koivunen, “MIMO-OFDM Joint Radar-Communications: Is ICI Friend or Foe?” *IEEE J. Sel. Topics Signal Process.*, vol. 15, no. 6, pp. 1393–1408, 2021.

[26] F. Wang and H. Li, “Power Allocation for Coexisting Multicarrier Radar and Communication Systems in Cluttered Environments,” *IEEE Trans. Signal Process.*, vol. 69, pp. 1603–1613, 2021.

[27] M. A. Islam, G. C. Alexandropoulos, and B. Smida, “Integrated Sensing and Communication with Millimeter Wave Full Duplex Hybrid Beamforming,” in *Proc. IEEE Int. Conf. Commun.*, 2022, pp. 4673–4678.

[28] X. Li, V. C. Andrei, U. J. Mönich, and H. Boche, “Optimal and Robust Waveform Design for MIMO-OFDM Channel Sensing: A Cramér-Rao Bound Perspective,” in *Proc. IEEE Int. Conf. Commun.*, 2023, pp. 3516–3521.

[29] L. Chen, Z. Wang, Y. Du, Y. Chen, and F. R. Yu, “Generalized Transceiver Beamforming for DFRC With MIMO Radar and MU-MIMO Communication,” *IEEE J. Sel. Areas Commun.*, vol. 40, no. 6, pp. 1795–1808, 2022.

[30] X. Yu, L. Tu, Q. Yang, M. Yu, Z. Xiao, and Y. Zhu, “Hybrid Beamforming in mmWave Massive MIMO for IoV With Dual-Functional Radar Communication,” *IEEE Trans. Veh. Technol.*, vol. 72, no. 7, pp. 9017–9030, 2023.

[31] M. F. Keskin, M. M. Mojahedian, J. O. Lacruz, C. Marcus, O. Eriksson, A. Giorgetti, J. Widmer, and H. Wymeersch, “Fundamental Trade-Offs in Monostatic ISAC: A Holistic Investigation Towards 6G,” 2024. [Online]. Available: https://arxiv.org/abs/2401.18011

[32] H. Ozen and G. M. Guvensen, “Interference and Beam Squint Aware TTD-Aided Beamforming for Dual Wideband Massive MIMO,” *IEEE Wireless Commun. Lett.*, vol. 13, no. 1, pp. 64–68, 2024.

[33] F. Gao, L. Xu, and S. Ma, “Integrated Sensing and Communications With Joint Beam-Squint and Beam-Split for mmWave/THz Massive MIMO,” *IEEE Trans. Commun.*, vol. 71, no. 5, pp. 2963–2976, 2023.

[34] U. B. Sarac and G. M. Guvensen, “On the Effects of Range-Doppler Processing for Target Detection in OFDM-Based RadCom,” *IEEE Commun. Lett.*, vol. 27, no. 7, pp. 1864–1868, 2023.

[35] G. Hakobyan and B. Yang, “A Novel Intercarrier-Interference Free Signal Processing Scheme for OFDM Radar,” *IEEE Trans. Veh. Technol.*, vol. 67, no. 6, pp. 5158–5167, 2018.

[36] H. Noh, H. Lee, and H. J. Yang, “ICI-Robust Transceiver Design for Integration of MIMO-OFDM Radar and MU-MIMO Communication,” *IEEE Trans. Veh. Technol.*, vol. 72, no. 1, pp. 821–838, 2023.

[37] Z. Xiao, R. Liu, M. Li, Q. Liu, and A. L. Swindlehurst, “A Novel Joint Angle-Range-Velocity Estimation Method for MIMO-OFDM ISAC Systems,” *IEEE Trans. Signal Process.*, vol. 72, pp. 3805–3818, 2024.

[38] F. Robey, D. Fuhrmann, E. Kelly, and R. Nitzberg, “A CFAR Adaptive Matched Filter Detector,” *IEEE Trans. Aerosp. Electron. Syst.*, vol. 28, no. 1, pp. 208–216, 1992.

[39] S. Fortunati, L. Sanguinetti, F. Gini, M. S. Greco, and B. Himed, “Massive MIMO Radar for Target Detection,” *IEEE Trans. Signal Process.*, vol. 68, pp. 859–871, 2020.

[40] M. Murthi and B. Rao, “Minimum Variance Distortionless Response (MVDR) Modeling of Voiced Speech,” in *Proc. Int. Conf. Acoustics Speech Signal Processing ’97*, vol. 3, 1997, pp. 1687–1690 vol.3.

[41] U. B. Sarac and G. M. Guvensen, “Knowledge-Aided and Adaptive Beam-Squint Aware MIMO-OFDM Radar Detectors for ISAC,” *TechRxiv*, June 17, 2024.

[42] M. I. Skolnik, *Radar Handbook*. McGraw-Hill, Inc., 1970.